

Research Paper

Tumor-penetrating Peptide Conjugated and Doxorubicin Loaded T₁-T₂ Dual Mode MRI Contrast Agents Nanoparticles for Tumor Theranostics

Lipeng Gao¹, Jing Yu¹, Yang Liu¹, Jinge Zhou¹, Lei Sun¹, Jing Wang¹, Jianzhong Zhu¹, Hui Peng², Weiyue Lu³, Lei Yu¹, Zhiqiang Yan¹✉, Yiting Wang¹✉

1. Institute of Biomedical Engineering and Technology, Shanghai Engineering Research Center of Molecular Therapeutics and New Drug Development, School of Chemistry and Molecular Engineering, East China Normal University, Shanghai 200062, China.
2. Key Laboratory of Polar Materials and Devices, Ministry of Education, School of Information Science and Technology, East China Normal University, Shanghai 200241, China.
3. Department of Pharmaceutics, School of Pharmacy, Fudan University & Key Laboratory of Smart Drug Delivery, Fudan University, Ministry of Education, Shanghai 201203, China.

✉ Corresponding author: zqyan@sat.ecnu.edu.cn, ytwang@nbic.ecnu.edu.cn

© Ivyspring International Publisher. This is an open access article distributed under the terms of the Creative Commons Attribution (CC BY-NC) license (<https://creativecommons.org/licenses/by-nc/4.0/>). See <http://ivyspring.com/terms> for full terms and conditions.

Received: 2017.05.18; Accepted: 2017.09.22; Published: 2018.01.01

Abstract

The conventional chemotherapeutics could not be traced in vivo and provide timely feedback on the clinical effectiveness of drugs.

Methods: In this study, a tumor-penetrating peptide RGERPPR (RGE) modified, Gd-DTPA conjugated, and doxorubicin (DOX) loaded Fe₃O₄@SiO₂@mSiO₂ nanoparticle drug delivery system (Fe₃O₄@SiO₂@mSiO₂/DOX-(Gd-DTPA)-PEG-RGE NPs) was prepared for tumor theranostics.

Results: The Fe₃O₄@SiO₂@mSiO₂/DOX-(Gd-DTPA)-PEG-RGE NPs showed a z-average hydrodynamic diameter of about 90 nm, and a pH-sensitive DOX release profile. The 3 T MRI results confirmed the relaxivity of the NPs ($r_1 = 6.13 \text{ mM}^{-1}\text{S}^{-1}$, $r_2 = 36.89 \text{ mM}^{-1}\text{S}^{-1}$). The in vitro cellular uptake and cytotoxicity assays on U87MG cells confirmed that the conjugation of RGERPPR played a significant role in increasing the cellular uptake and cytotoxicity of the NPs. The near-infrared fluorescence in vivo imaging results showed that the NPs could be significantly accumulated in the U87MG tumor tissue, which should result from the mediation of the tumor-penetrating peptide RGERPPR. The MRI results showed that the NPs offered a T₁-T₂ dual mode contrast imaging effect which would lead to a more precise diagnosis. Compared with unmodified NPs, the RGE-modified NPs showed significantly enhanced MR imaging signal in tumor tissue and antitumor effect, which should also be attributed to the tumor penetrating ability of RGERPPR peptide. Furthermore, the Hematoxylin and Eosin (H&E) staining and TUNEL assay proved that the NPs produced obvious cell apoptosis in tumor tissue.

Conclusions: These results indicated that Fe₃O₄@SiO₂@mSiO₂/DOX-(Gd-DTPA)-PEG-RGE NPs are an effective targeted delivery system for tumor theranostics, and should have a potential value in the personalized treatment of tumor.

Key words: Theranostics, Tumor penetrating peptide, T₁-T₂ dual mode MRI, pH-sensitive release, Fe₃O₄@SiO₂@mSiO₂/DOX-(Gd-DTPA)-PEG-RGE NPs

Introduction

Cancer is one of the leading causes of death worldwide and seriously threaten human health [1,

2]. Currently, chemotherapy is still one of the most effective ways to treat cancer clinically [3]. However,

the traditional chemotherapy is difficult to distinguish between cancer cells and normal cells, causing serious side effects to patients. Moreover, because of the conventional chemotherapeutic drugs cannot be traced in the body, their distribution in the tumor tissue cannot be known in real time. Therefore, they cannot provide timely feedback for the clinical effectiveness of the drug. This is also the main reason why personalized treatment of cancer cannot be achieved. Many scientists believe that this is the major problem in the current clinical chemotherapy of tumor, which needs to be urgently addressed by an effective technology.

Theranostics refer to the simultaneous integration of diagnosis and therapy [4, 5]. A variety of nanomedicine platforms are exploited for theranostics, mainly including organic nanoparticles (NPs) [6-9] and inorganic NPs [10-13]. Especially, inorganic NPs have attracted much attention for their easy preparation and modification in the past decades. For example, mesoporous silica (mSiO₂) NPs [14], as one of the most representative inorganic nanocarriers, have been explored for drug delivery, molecular imaging, and synergistic cancer therapy, on account of their large specific surface area, low toxicity, easy functionalization, etc. Pan et al. reported that a cell membrane penetrating peptide TAT modified MSNs significantly enhanced the anticancer activity of the loaded doxorubicin [15]. Li et al. developed monodisperse mesoporous manganese silicate coated silica NPs (MMSSNs) as a highly efficient T₁-weighted MRI contrast agent and drug carrier for cancer diagnosis and chemotherapy [16].

Magnetic resonance imaging (MRI) is an excellent clinical imaging technique for the noninvasive detection of tumor. To improve the imaging contrast between normal and diseased tissues, contrast agents are employed to change proton relaxation rates [17, 18]. Nowadays, the MRI contrast agents are generally in the form of T₁-positive and T₂-negative contrast agents. T₁ contrast agents, such as gadolinium (Gd)-based chelates (e.g., Gd-DTPA) [19, 20], can facilitate the spin-lattice relaxation of protons and provide a brighter MR image. T₂ contrast agents, such as superparamagnetic iron oxide (SPIO) NPs (e.g., Feridex) [21], can cause protons in the vicinity to undergo spin-spin relaxation and produce a darker MR image. However, such single mode contrast agents still have disadvantages. The Gd-based T₁-positive contrast agents have suffered from their short body circulation time due to their low molecular weights, making it hard to acquire high-resolution images, which requires a long scan time [22]. Besides, the clinical use of T₂ contrast agents is quite limited due to their inherent darkening

contrast effect and magnetic susceptibility artifacts [23]. Consequently, the T₁-T₂ dual model contrast agents are becoming attractive because this new type of contrast agents can offer complementary diagnostic information, effectively eliminate false errors, achieve artifact-free imaging [24, 25], and lead to a more precise diagnosis. For instance, Yang et al. prepared T₁-T₂ dual model contrast agents (Fe₃O₄@SiO₂(Gd-DTPA)-RGD NPs) significantly improved the diagnostic accuracy [26].

Tumor targeted drug delivery systems (TDDS), especially ligand-modified active targeting delivery systems, have received much attraction due to their advantages of precise tumor targeting, enhanced antitumor efficacy and reduced systemic side effects [27]. Tumor targeting ligands, such as peptides, antibodies and their fragments, play a key role in tumor targeting. They can mediate tumor cellular uptake of the nanoparticle delivery system by interacting with receptors overexpressed in tumor tissues [28]. Neuropilin-1 (NRP-1) is a receptor overexpressed on both U87MG cells and tumor vascular endothelium [29]. RGERPPR peptide, a specific ligand of NRP-1, is a tumor-penetrating peptide with the ability to penetrate tumor vessels and tumor tissues [30-32]. Several reports have proved that RGERPPR-modified drug delivery system could penetrate into deep tumor tissue and significantly enhance the antitumor effect of the loaded drug [33, 34].

In this study, we prepared an RGERPPR (RGE) modified, Gd-DTPA conjugated, and doxorubicin (DOX) loaded Fe₃O₄@SiO₂@mSiO₂ nanoparticle drug delivery system (Fe₃O₄@SiO₂@mSiO₂/DOX-(Gd-DTPA)-PEG-RGE NPs) for tumor theranostics (Figure 1). This study was carried out to prove our hypothesis that the prepared NPs were targeted to tumor tissue by the EPR effect and RGE mediation, thereby enhancing the Gd-DTPA/Fe₃O₄ based T₁-T₂ dual mode imaging response and the antitumor effect of loaded DOX. We characterized the NPs by TEM, DLS, FTIR, ICP-OES, XRD and MR imaging, and further evaluated their function of tumor diagnosis and treatment on U87MG cells in vitro and in vivo. Our results showed that this NPs could be used as an effective platform for tumor theranostics.

Materials and Methods

Materials

Igepal CO-520 (Polyoxyethylene (5) nonylphenylether, branched), TEOS (Tetraethyl orthosilicate), CTAC (Hexadecyltrimethylammonium chloride), APTES ((3-aminopropyl)triethoxysilane), DTPA (Diethylenetriaminepentaacetic acid), FeCl₃·

6H₂O, GdCl₃·6H₂O, NHS (N-hydroxysuccinimide) and N,N'-dimethylaminopyridine were supplied from Sigma-Aldrich, Inc. EDC (N-(3-dimethylaminopropyl)-N'-ethylcarbodiimide) was purchased from EMD Chemicals Inc. (Darmstadt, Germany). Thiolated RGERPPR (C-RGERPPR) was obtained from Shanghai Top-peptide Co., Ltd. Mal-PEG3400-COOH and mPEG5000-COOH were purchased from Shanghai Yare Biotech, Inc. CCK-8 (Cell Counting Kit-8) was purchased from DOJINDO Laboratories chemical technology (Shanghai) Co., LTD. DiO (3,3'-dioctadecyloxycarbocyanine, perchlorate) and DiR (1,1'-dioctadecyl-3,3',3'-tetramethyl indotricarbocyanine Iodide) were purchased from Tianjin Biolite Biotech Co., LTD. Hoechst 33342 was purchased from Beyotime Institute of Biotechnology. All other chemicals and reagents were commercially available and directly used.

U87MG cell line was obtained from Shanghai Institute of Cell Biology. This cell was cultured in Dulbecco's Modified Eagle Medium (DMEM, Gibco Co., USA) supplemented with 10% fetal bovine serum (FBS, Gibco Co., USA) at 37 °C in a humidified atmosphere of 5% CO₂ and 95% air.

Balb/c nude mice were obtained from SLAC Ltd (Shanghai, China) and kept under SPF conditions. All experiments involving animals were performed in accordance with the guidelines of the Institutional Animal Care and Use Committee (IACUC) of East China Normal University.

Synthesis of Fe₃O₄@SiO₂@mSiO₂/DOX-(Gd-DTPA)-PEG-RGE

Synthesis of iron-oleate complex

The metal-oleate complex was prepared by reacting metal chlorides with sodium oleate. In a typical synthesis of iron-oleate complex [35], 10.8 g of FeCl₃·6H₂O (40 mmol) and 36.5 g of sodium oleate (120 mmol) was dissolved in a mixed solvent of 80 mL ethanol, 60 mL distilled water and 140 mL hexane. The resulting solution was heated to 70 °C and kept at that temperature for 4 hours. When the reaction was completed, the upper organic layer containing the iron-oleate complex was washed three times with 30 mL distilled water in a separatory funnel. After that, hexane was evaporated off to obtain the iron-oleate complex in a waxy solid form.

Synthesis of iron oxide nanocrystals

The monodisperse iron oxide (magnetite) nanocrystals with a particle size of 12 nm were synthesized according to the following procedure [35]. 36 g of the synthesized iron-oleate complex (40 mmol) and 5.7 g of oleic acid (20 mmol) were dissolved in 200 g of 1-octadecene at room

temperature. The reaction mixture was heated to 320 °C with a constant heating rate of 3.3 °C/min, and then kept at that temperature for 60 min. When the reaction temperature reached 320 °C, a severe reaction occurred and the initial transparent solution became turbid and brownish black. The resulting solution containing the nanocrystals was then cooled to room temperature, and 500 mL of ethanol was added to the solution to precipitate the nanocrystals, which were then separated out by centrifugation.

Synthesis of Fe₃O₄@SiO₂ NPs

The monodisperse Fe₃O₄@SiO₂ NPs was prepared through a simplified method [36, 37]. The present process featured a careful and precise control of the injecting rate of silica source and other parameters. 8 mL Igepal CO-520 (NP-5) was dispersed in 170 mL cyclohexane in a 250 mL three-necked flask and stirred for 30 min. Subsequently, 10 mL monodisperse oleic acid capped Fe₃O₄-cyclohexane solution (0.688 mg/mL) was injected into the cyclohexane/NP-5 mixture. 1.3 mL Ammonia (30%) was added dropwise, and the system was sealed and stirred for 5 min. 1.5 mL TEOS was delivered into the system at a precisely controlled rate of 1 mL/h by using a Longer Pump (LSP02-1B). The mixture was sealed and kept stirring for 96 hours at room temperature before adding methanol to collect the solid particles. The product was firstly precipitated with excess hexane and collected by magnetic separation. Then the particles were re-dispersed in ethanol under ultrasonic treatment, precipitated with excess hexane, and collected by magnetic separation. The as-synthesized Fe₃O₄@SiO₂ particles were washed three times to remove excess NP-5. The as-obtained Fe₃O₄@SiO₂ could be well dispersed in deionized water (20 mL).

Synthesis of Fe₃O₄@SiO₂@mSiO₂

For the synthesis of Fe₃O₄@SiO₂@mSiO₂, a procedure from the literature was used with some modification [15, 38]. 2g CTAC and 82 μL TEA (triethanolamine) were dissolved in turn in 20 mL Fe₃O₄@SiO₂ solution at 95°C under intensive stirring. After 1h, 1.5 mL of TEOS was added dropwise, and the resulting mixture was stirred for another 1h. The products were collected by centrifugation and washed for several times with ethanol to remove the residual reactants. Then, the collected products were extracted for 3 h with a 1 wt% solution of NaCl in methanol at room temperature. This procedure was repeated five times to remove the template CTAC. After washing twice with ethanol, the Fe₃O₄@SiO₂@mSiO₂ were redispersed in 50 mL of ethanol.

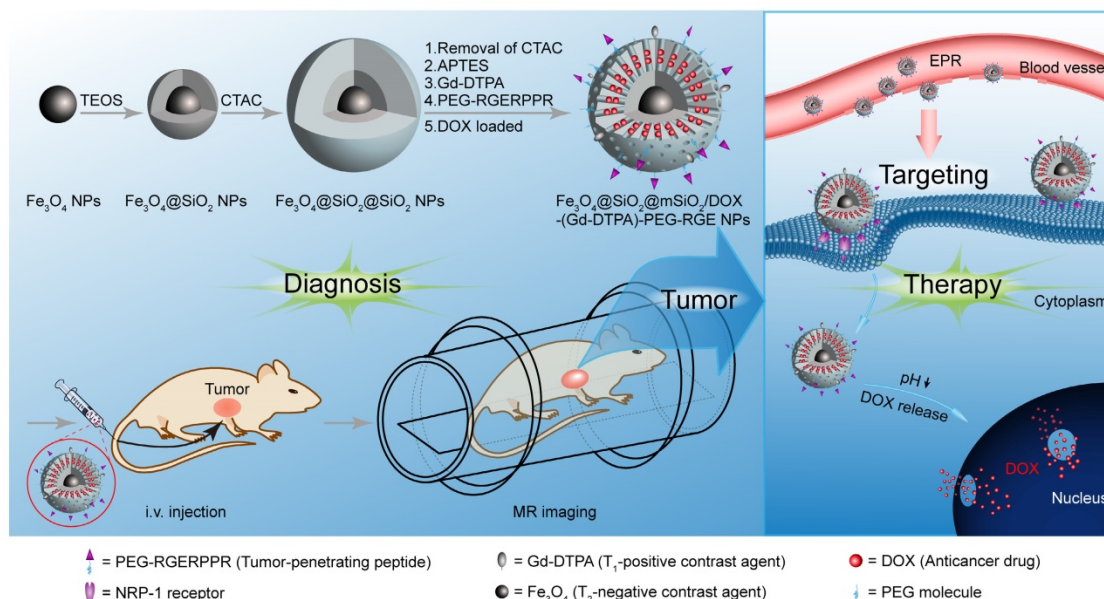


Figure 1. Schematics of the MR imaging of the $\text{Fe}_3\text{O}_4@SiO_2@mSiO_2/DOX-(Gd-DTPA)-PEG-RGE$ NPs.

Synthesis of $\text{Fe}_3\text{O}_4@SiO_2@mSiO_2-NH_2$

The surface of $\text{Fe}_3\text{O}_4@SiO_2@mSiO_2$ was functionalized with amine groups by treating with APTES [15]. 50 mg $\text{Fe}_3\text{O}_4@SiO_2@mSiO_2$ were dispersed in 50 mL of ethanol, and then the solution was refluxed for 4 h, followed by the addition of 0.5 mL APTES. After centrifugation and washing with water, amine-functionalized $\text{Fe}_3\text{O}_4@SiO_2@mSiO_2$ were obtained and stored at 4 °C before use.

Synthesis of $\text{Fe}_3\text{O}_4@SiO_2@mSiO_2-(Gd-DTPA)$

The $\text{Fe}_3\text{O}_4@SiO_2@mSiO_2-NH_2$ was further functionalized by treatment with DTPA (Figure S1) [26]. 150 mg DTPA, 80 mg NHS and 130 mg EDC were dispersed in 20 mL of anhydrous DMF. Then 20 mg $\text{Fe}_3\text{O}_4@SiO_2@mSiO_2-NH_2$ and 80 mg DMAP were added and stirred for 12 h and washing with distilled water several times. The prepared $\text{Fe}_3\text{O}_4@SiO_2@mSiO_2-(DTPA)$ were dispersed in 15 mL Tris-HCl buffer solution (0.05 M, pH 7.4). Then, 160 mg $GdCl_3 \cdot 6H_2O$ were added, and the mixed solution was stirred overnight. After washing with distilled water several times, $\text{Fe}_3\text{O}_4@SiO_2@mSiO_2-(Gd-DTPA)$ was stored at 4 °C before use.

Synthesis of

$\text{Fe}_3\text{O}_4@SiO_2@mSiO_2-(Gd-DTPA)-PEG-RGE$

RGERPPR-PEG-COOH was synthesized by reaction thiolated RGERPPR with Mal-PEG3400-COOH as described previously [34, 39]. The reaction solution was purified by dialysis (M.W. CO 3.5K) against distilled water, followed by lyophilization.

The structure was verified by ^1H-NMR and FTIR (Figure S2).

RGERPPR-PEG-COOH was covalently conjugated to amine-functionalized $\text{Fe}_3\text{O}_4@SiO_2@mSiO_2-(Gd-DTPA)-NH_2$ through the -COOH group by using the cross-linking reagents, EDC and NHS (Figure S1) [15]. 2 mmol RGERPPR-PEG-COOH was dissolved in phosphate buffered saline (PBS) solution (pH 7.4) followed by the addition of 3 mmol EDC and 6 mmol NHS. The mixture was then stirred at room temperature for 60 min to activate the carboxylic group. Then, 20 mL PBS solution of $\text{Fe}_3\text{O}_4@SiO_2@mSiO_2-(Gd-DTPA)-NH_2$ (1 mg/mL) was added, and the mixture was gently stirred at room temperature for 24 h. After washing with distilled water several times, $\text{Fe}_3\text{O}_4@SiO_2@mSiO_2-(Gd-DTPA)-PEG-RGE$ were stored at 4 °C before use.

Loading of DOX into

$\text{Fe}_3\text{O}_4@SiO_2@mSiO_2-(Gd-DTPA)-PEG-RGE$

$\text{Fe}_3\text{O}_4@SiO_2@mSiO_2-(Gd-DTPA)-PEG-RGE$ (5 mg) were dispersed into 20 mL of DOX solution in PBS (0.5 mg/mL) under stirring overnight in dark conditions [14]. DOX-loaded NPs were centrifuged, and the supernatant was collected for UV-vis spectrophotometry (UV-1800, Shimadzu) at 480 nm to determine the unloaded DOX. For in vitro and in vivo applications, the $\text{Fe}_3\text{O}_4@SiO_2@mSiO_2/DOX-(Gd-DTPA)-PEG-RGE$ were dispersed in 0.5 mL of phosphate buffer solution (PBS, 10 mM, pH 7.4) and filtered using a 0.22 μm cellulose acetate syringe filter (Millex-GV, Millipore).

Characterization of Fe₃O₄@SiO₂@mSiO₂/DOX-(Gd-DTPA)-PEG-RGE NPs

The morphology of Fe₃O₄ NPs, Fe₃O₄@SiO₂ NPs, Fe₃O₄@SiO₂@SiO₂ NPs, and Fe₃O₄@SiO₂@mSiO₂ NPs were observed using transmission electron microscopy (TEM). The TEM study was carried out using a JEM-2100 (Hitachi, Tokyo, Japan) electron microscope operating at an accelerating voltage of 75 kV.

The particle sizes of NPs was determined by dynamic light scattering (DLS) using a Mastersizer2000 (Malvern Instruments Inc, UK) equipped with He-Ne laser (4 mW, 633 nm) light source and 90° angle scattered-light collection configuration.

The Z-potential analysis of the particles was performed by DLS. The NPs were loaded into a universal dip cell before recording. The experiment was repeated in triplicate for each sample.

Fourier transform infrared spectrometer (FTIR) spectra were collected using a Nicolet Nexus 670 FTIR spectrometer. The samples were pelletized with KBr before measurements.

The concentration of Fe and Gd element in the particles was determined by inductively coupled plasma optical emission spectroscopy (ICP-OES, IRIS Intrepid II XSP, Thermo Fisher Scientific, USA).

X-ray diffraction (XRD) spectra were collected from 10° to 70° (2θ), with a step of 0.02° by using a Ni filtered Cu K_α (λ = 1.5418 Å) radiation source (D/Max-2550V, Rigaku Co.). The JCPDS PDF database was utilized for phase identification.

The ¹H-NMR spectra of Mal-PEG3400-COOH and RGERPPR-PEG3400-COOH in deuterated chloroform (CDCl₃) were recorded with a Bruker spectrometer at 400 MHz.

Relaxivity measurements

The longitudinal relaxation rates (r₁) and transverse relaxation rates (r₂) were measured to evaluate the ability of contrast agents for MRI [40]. To assess the relaxation characteristics of the Fe₃O₄@SiO₂@mSiO₂/DOX-(Gd-DTPA)-PEG-RGE NPs as a T₁-T₂ dual MR contrast agents, the T₁ relaxation times and T₂ relaxation times of NPs at different Gd concentrations were performed with a 3T MRI (SIEMENS MAGNETOM Trio I-class, Germany). All samples were diluted in normal saline (0.9% w/v NaCl, pH 7.4). T₁-weighted MR images were acquired using a conventional spin-echo sequence under the following parameters: TR = 500 ms, TE = 14 ms, α = 90°, slice thickness = 2 mm, and image matrix = 384 × 384. T₂-weighted MR images were obtained by using a fast spin-echo sequence under the following parameters: TR = 4000 ms, TE = 75 ms, α = 120°, slice

thickness = 2 mm, and image matrix = 384 × 384. The specific relaxivity values of r₁ and r₂ were calculated from the slope of the linear curve of inverse relaxation time (1/T₁ and 1/T₂) vs the Gd concentration (mM).

Release of DOX from NPs in vitro

The Fe₃O₄@SiO₂@mSiO₂/DOX-(Gd-DTPA)-PEG-RGE NPs were suspended in fresh PBS (pH 7.4, pH 6.5 and pH 5.5) with a final concentration of 0.5 mg/mL and packed in 5 mL of centrifuge tube. Then they were shaken horizontally at 120 min⁻¹ with an incubator shaker (HZ-8812S, Scientific and Educational Equipment plant, China) at 37 °C. The sample was withdrawn at predetermined time points and centrifuged at 12,000 rpm for 10 min. Finally, the drug concentration was determined by UV-vis spectrophotometry (UV-1800, Shimadzu).

Cytotoxicity assays

The in vitro cytotoxicity of NPs was investigated by the CCK-8 assay according to the published protocols with modifications [41]. U87MG cells (3 × 10³) were seeded in 96-well plates and incubated for 24 h. Then serial dilutions of DOX, Fe₃O₄@SiO₂@mSiO₂/DOX-(Gd-DTPA)-PEG NPs and Fe₃O₄@SiO₂@mSiO₂/DOX-(Gd-DTPA)-PEG-RGE NPs were added to the plate (100 μL/well). Following incubation for up to 48 hours, the cells were treated with 10 μL of CCK-8 solution and cultured for 4 h. The absorbance was measured with a microplate reader (SpectraMax M5, Molecular Devices, USA) at 450 nm. The survival rate was calculated using the following formula: viability rate (%) = (OD_{test group} - OD_{Blank}) / (OD_{control group} - OD_{Blank}) × 100%.

Tumor cellular uptake of NPs in vitro

Preparations of Fe₃O₄@SiO₂@mSiO₂/DiO-(Gd-DTPA)-PEG-RGE NPs

Fe₃O₄@SiO₂@mSiO₂/DiO-(Gd-DTPA)-PEG-RGE NPs were prepared as follows [42]. Briefly, DiO and the NPs were suspended in the mixture of methylene chloride and acetone (3:1, v/v), which was then removed by rotary evaporation to obtain the Fe₃O₄@SiO₂@mSiO₂/DiO-(Gd-DTPA)-PEG-RGE NPs. Then the NPs were resuspended in water, and performed with G50 gel chromatography to remove free DiO with AKTA purifier (GE Healthcare).

DiR was loaded into the NPs using the same protocol with DiO.

Cellular uptake

Cellular uptake study was performed with the U87MG cell line. Cells were seeded in a glass-bottom dish or 6-well plates at a density of 3 × 10⁴ cells/mL and cultured for 24 h. The cells were divided into 3

groups: RGE-modified NPs group, NRP-1 inhibitor plus RGE-modified NPs group, and unmodified NPs group. For the NRP-1 inhibitor plus RGE-modified NPs group, the cells were first cultured in the presence of NRP-1 inhibitor EG00229 (R&D Systems) at 100 μ M. The three groups of cells were washed with phosphate buffered saline (PBS) and incubated with different concentrations of their corresponding NPs for 2 h.

To observe the cellular uptake of NPs qualitatively, the treated cells were washed three times with cold PBS, fixed with 4 % paraformaldehyde, stained with Hoechst33342 and observed using a confocal laser scanning microscope (CLSM, TCS SP5, Leica, Germany).

For quantitative analysis, the treated cells were washed with cold PBS, trypsinized and harvested by centrifugation at 1200 rpm for 5 min. The cells were resuspended in 200 μ L PBS and filtered through a 40 mm nylon mesh to remove cell aggregates. The cell suspension was then analyzed by flow cytometry (Guava easyCyte, USA).

Building of tumor animal model

Male nude mice (6 weeks) were inoculated subcutaneously with U87MG cells (3×10^6 cells in 0.1 mL PBS). Tumor diameters were measured every two days using a sliding caliper. The tumor volume (TV) was calculated according to the formula $TV = (L \times W^2)/2$, where L and W were the lengths of the major and minor diameters, respectively.

Near infrared fluorescence in vivo imaging

The accumulation of $Fe_3O_4@SiO_2@mSiO_2$ -(Gd-DTPA)-PEG-RGE NPs in tumor tissue was evaluated by near-infrared fluorescence in vivo imaging study. The subcutaneous U87MG tumor-bearing mice ($n = 3$) were i.v. injected with 100 μ L of $Fe_3O_4@SiO_2@mSiO_2$ /DiR-(Gd-DTPA)-PEG-RGE NPs via the tail vein. At pre-injection and 2, 4, 8, 12, 24, 48 h post-injection, the mice were anesthetized and the fluorescent images were captured using an in vivo imaging system (In-Vivo FX PRO, Bruker) equipped with a DiR filter sets (excitation/emission, 730/790 nm). The tumor tissues were harvested and weighed at the end of the experiment. Pharmacokinetic profile of $Fe_3O_4@SiO_2@mSiO_2$ /DiR-(Gd-DTPA)-PEG-RGE NPs in tumor-bearing nude mice was obtained based on the semi-quantitative ROI analysis of the fluorescent images.

T₁-T₂ dual mode MR imaging in vivo

The U87MG tumor-bearing mice ($n = 3$) were anesthetized by intraperitoneal injection of pentobarbital sodium (50 μ L, 2.5%, 50 mg/kg). MR images were acquired on a 3T MRI (SIEMENS

MAGNETOM Trio I-class, Germany) scanner with an animal coil. $Fe_3O_4@SiO_2@mSiO_2$ /DOX-(Gd-DTPA)-PEG-RGE NPs were injected at a dose of 0.07 mmol-Gd/kg body weight via the tail vein, and $Fe_3O_4@SiO_2@mSiO_2$ /DOX-(Gd-DTPA)-PEG NPs were as the control with the same dose. Scans were performed at different time points. T₁-weighted MR images were acquired using a conventional spin-echo sequence with the following parameters: TR = 400 ms, TE = 12 ms, $\alpha = 90^\circ$, slice thickness = 1 mm, and image matrix = 256×256 . T₂-weighted MR images were obtained by using a fast spin-echo sequence under the following parameters: TR = 3500 ms, TE = 71 ms, $\alpha = 120^\circ$, slice thickness = 1 mm, and image matrix = 256×256 . The MRI T₁ and T₂ signal intensities (SI) within the regions of interest (ROIs) were measured three times before and after injection of the NPs. The relative enhancement signal intensity (RESI) was calculated according to the following formula: $RESI (\%) = SI_{contrast}/SI_{pre} \times 100\%$, in which, $SI_{contrast}$ is the signal intensity of tumor after the injection, and SI_{pre} is that before the injection.

Pharmacokinetic study

The pharmacokinetic behavior of $Fe_3O_4@SiO_2@mSiO_2$ /DiR-(Gd-DTPA)-PEG NPs and $Fe_3O_4@SiO_2@mSiO_2$ /DiR-(Gd-DTPA)-PEG-RGE NPs were evaluated as follows. The male SD rats (6-8 weeks) was randomly divided into 2 groups ($n = 3$). The two NPs (at the DiR dose of 100 μ g) were i.v. injected via tail vein. Blood (200 μ L) were collected at 10 min, 30 min, 1 h, 2 h, 4 h, 8 h, 12 h, 24 h and 48 h post-injection, respectively. The NPs in blood samples were quantified by measuring the concentration of DiR with a Hitachi F-4500 fluorescence spectrophotometer (Ex/Em=748/780 nm).

Bio-distribution study

The U87MG tumor-bearing mice ($n = 3$) were i.v. injected of $Fe_3O_4@SiO_2@mSiO_2$ /DiR-(Gd-DTPA)-PEG NPs and $Fe_3O_4@SiO_2@mSiO_2$ /DiR-(Gd-DTPA)-PEG-RGE NPs (at the DiR dose of 10 μ g) via the tail vein. At 8 h post-injection, the mice were sacrificed and performed of heart perfusion. After that, the tumor tissues and main organs (including heart, liver, spleen, lung, and kidney) were collected. After tissue homogenization with saline, the DiR in tissue samples were quantified by a Hitachi F-4500 fluorescence spectrophotometer with Ex/Em=748/780 nm at room temperature.

The antitumor effect in vivo

The tumor-bearing mice were randomly divided into four groups ($n = 6$): 1) saline; 2) DOX (5 mg/kg); 3) $Fe_3O_4@SiO_2@mSiO_2$ /DOX-(Gd-DTPA)-PEG NPs (5 mg/kg of DOX); 4) $Fe_3O_4@SiO_2@mSiO_2$ /DOX-

(Gd-DTPA)-PEG-RGE NPs (5 mg/kg of DOX). The drug administration was started when the tumor volume reached 100-120 mm³ [43]. The four groups of mice were administered intravenously via tail-vein and the treatments were given only once. The body weight and tumor volume of the mice were measured every two days until the TV of the saline group reached 3000 mm³, when all the mice were terminated.

Histological verification

H&E staining

When the chemotherapy was ended, U87MG tumor-bearing mice (n = 3) were sacrificed and the histocompatibility was evaluated by Hematoxylin and Eosin (H&E) staining [44]. Tumor tissues and main organs were collected and immediately fixed using 10% formalin solution and paraffin embedded tissues. Routine paraffin sections and H&E staining were performed according to standard clinical pathology protocols.

TUNEL assay

Tissue apoptotic cells were detected with TUNEL (TdT-mediated dUTP Nick-End Labeling) using a commercial kit (No. 12156792910; Roche, Switzerland) according to the manufacturer's protocol. TUNEL assay was performed for paraffin sections fixed with 4% paraformaldehyde and processed [45]. The sections were analyzed under a fluorescent microscope (Olympus, IX71, Japan).

Tumor-penetrating ability of NPs

Immunofluorescence method was used to investigate the tumor-penetrating ability of Fe₃O₄@SiO₂@mSiO₂/DiO-(Gd-DTPA)-PEG-RGE NPs. The Fe₃O₄@SiO₂@mSiO₂/DiO-(Gd-DTPA)-PEG-RGE NPs were i.v. injected to U87MG tumor-bearing mice (n = 3). The mice were sacrificed 8 h post-injection, and the tumor tissues and main organs (including heart, liver, spleen, lung, and kidney) were collected, fixed, dehydrated, and frozen in acetone/dry ice mixture. The frozen samples were further cut to sections (10 μm) with a cryostat (CM3050 S, Leica, Germany). The sections were stained with rat anti-mouse CD31 (1:10, R&D Systems), followed by rhodamine labeled goat anti-rat IgG (1:100, Santa Cruz) and Hoechst33342, and then observed using a confocal laser scanning microscope (CLSM, TCS SP5, Leica, Germany).

Statistical analysis

Statistical differences were evaluated with two-tailed student's t-test for data with two groups and one-way ANOVA for data with over three groups

(GraphPad Prism v7.00, GraphPad Software, San Diego, CA, USA). The difference was considered to be significant when P < 0.05 (*), P < 0.01 (**) and P < 0.001 (***).

Results

Characterization of the NPs by TEM, DLS, FTIR, ICP-OES and XRD

TEM and DLS

As depicted in the TEM images (Figure 2A, Figure 2B, Figure 2C and Figure 2D), the Fe₃O₄ NPs, Fe₃O₄@SiO₂ NPs, Fe₃O₄@SiO₂@SiO₂ NPs and Fe₃O₄@SiO₂@mSiO₂ NPs all showed a high uniformity particle size distribution. Their diameters are about 12 nm, 50 nm, 77 nm and 75 nm, respectively. The thicknesses of SiO₂ shell and mSiO₂ shell are about 19 nm and 12.5 nm, respectively. Furthermore, their particle size distributions examined by DLS are shown in the insets. Their Z-mean diameters were about 15 nm, 57 nm, 83 nm and 81 nm, and the PDIs were 0.133, 0.194, 0.361 and 0.338, respectively. The particle size of NPs observed by TEM was smaller than that determined by DLS. We speculated that the latter represents their hydrodynamic diameter, whereas the former represents the collapsed diameter after water evaporation. The result is consistent with previous report [46]. The Z-potential of Fe₃O₄@SiO₂@mSiO₂ NPs, Fe₃O₄@SiO₂@mSiO₂-NH₂ NPs, Fe₃O₄@SiO₂@mSiO₂-(Gd-DTPA)-PEG NPs and Fe₃O₄@SiO₂@mSiO₂-(Gd-DTPA)-PEG-RGE NPs were about - 19.6 mV, + 26.1 mV, - 3.8 mV and + 11.7 mV, respectively.

FTIR

As shown in the FTIR spectra presented in Figure 2E, the absorption peak at 580 cm⁻¹ belongs to the stretching vibration mode of Fe-O bonds in Fe₃O₄. After SiO₂ shell coating, the new band at 1090 cm⁻¹ should be assigned to the asymmetric vibration modes and the one at 463 cm⁻¹ should be the deformation vibration of the Si-O bond. Further, the outer SiO₂ shell coating via CTAC produced new peaks at 3000-2800 cm⁻¹, which should be assigned to the -CH₂ in CTAC. The new peaks are disappeared in the FTIR spectra of Fe₃O₄@SiO₂@mSiO₂, suggesting the complete removal of CTAC. That ensured the high biocompatibility of the carriers and the loading of anticancer drugs. The FTIR spectra of Fe₃O₄@SiO₂@mSiO₂-(Gd-DTPA) showed a significantly weaken band of Si-O at 1090 cm⁻¹, a new absorption band at around 3430 cm⁻¹ due to the stretching vibration of the -OH (COOH), and a C=O stretch band at around 1632 cm⁻¹. The FTIR spectra of Fe₃O₄@SiO₂@mSiO₂-(Gd-DTPA)-PEG-RGE showed

strong broad peaks at around 3400 cm^{-1} , which is consistent with a large amount of surface -OH (COOH). The broad peaks at around 3415 cm^{-1} should be attributed to the stretching and bending vibrations of N-H. The reappearance of strong bands at around $3000\text{--}2800\text{ cm}^{-1}$ corresponding to the -CH_2 (PEG) stretching vibrations. Moreover, the C=O stretch band at around 1632 cm^{-1} and the C-N bands at around $1439\text{--}1292\text{ cm}^{-1}$ are found in this FTIR spectrum. These

absorption bands provide strong evidence that Gd-DTPA and RGERPPR-PEG3400-COOH have been successfully conjugated to $\text{Fe}_3\text{O}_4@\text{SiO}_2@\text{mSiO}_2$ NPs.

The Gd content was about 0.93 mmol-Gd per gram of $\text{Fe}_3\text{O}_4@\text{SiO}_2@\text{mSiO}_2/\text{DOX}-(\text{Gd-DTPA})\text{-PEG-RGE}$ NPs as determined by ICP-OES, and the Gd/Fe molar ratio was about 1.52:1. The results suggested the successful conjugated of Gd-DTPA.

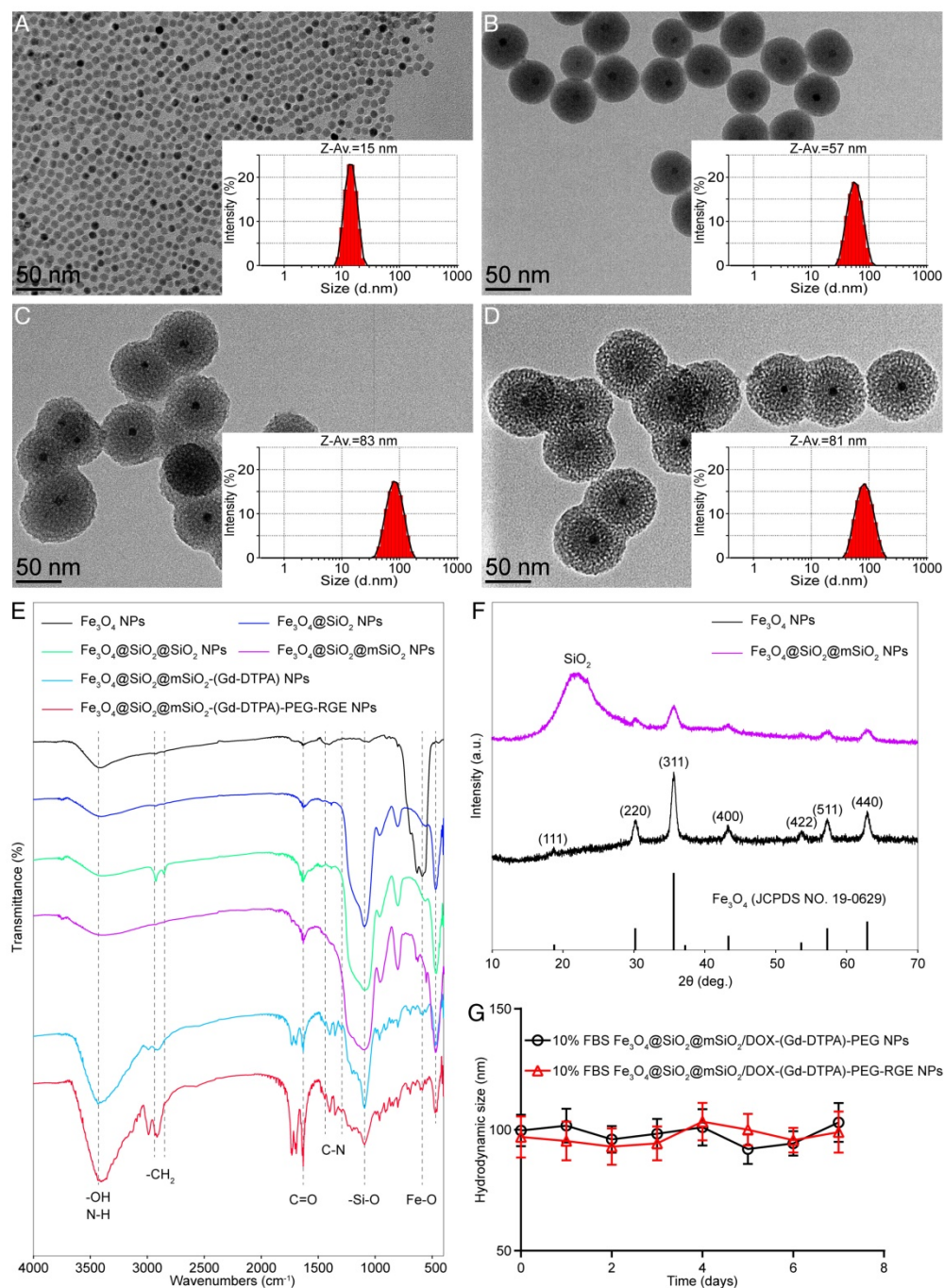


Figure 2. Characterization of the $\text{Fe}_3\text{O}_4@\text{SiO}_2@\text{mSiO}_2/\text{DOX}-(\text{Gd-DTPA})\text{-PEG-RGE}$ NPs. Typical TEM images of Fe_3O_4 NPs (A), $\text{Fe}_3\text{O}_4@\text{SiO}_2$ NPs (B), $\text{Fe}_3\text{O}_4@\text{SiO}_2@\text{SiO}_2$ NPs (C) and $\text{Fe}_3\text{O}_4@\text{SiO}_2@\text{mSiO}_2$ NPs (D) and their size distribution (inset). (E) FTIR spectrum of Fe_3O_4 NPs, $\text{Fe}_3\text{O}_4@\text{SiO}_2$ NPs, $\text{Fe}_3\text{O}_4@\text{SiO}_2@\text{SiO}_2$ NPs, $\text{Fe}_3\text{O}_4@\text{SiO}_2@\text{mSiO}_2$ NPs, $\text{Fe}_3\text{O}_4@\text{SiO}_2@\text{mSiO}_2-(\text{Gd-DTPA})$ NPs and $\text{Fe}_3\text{O}_4@\text{SiO}_2@\text{mSiO}_2-(\text{Gd-DTPA})\text{-PEG-RGE}$ NPs. (F) X-ray diffraction patterns of Fe_3O_4 NPs and $\text{Fe}_3\text{O}_4@\text{SiO}_2@\text{mSiO}_2$ NPs. The standard XRD pattern of Fe_3O_4 (JCPDS No. 19-0629) is shown by solid bars. (G) The stability of $\text{Fe}_3\text{O}_4@\text{SiO}_2@\text{mSiO}_2/\text{DOX}-(\text{Gd-DTPA})\text{-PEG-RGE}$ NPs in serum.

In order to conjugate Gd-DTPA and RGERPPR-PEG-COOH to the surface of $\text{Fe}_3\text{O}_4@\text{SiO}_2@\text{mSiO}_2\text{-NH}_2$ NPs, the amount of amine moieties on the NP surface was determined using the standard Fmoc quantification protocol [47]. The density of the amine groups on the NPs was determined to be about 7.2×10^{-4} mol/g. After the Gd-DTPA conjugation, the amount of the remaining amine groups on the $\text{Fe}_3\text{O}_4@\text{SiO}_2@\text{mSiO}_2\text{-(Gd-DTPA)-NH}_2$ NPs was quantified to be 2.1×10^{-4} mol/g, with about 29.1 mol% free amines available on the surface of the NP for further conjugation modification. The amount of the remaining amine groups after RGERPPR-PEG-COOH conjugation was measured to be 1.3×10^{-5} mol/g (about 1.8 mol%). The results indicated that most of the surface amine groups on the $\text{Fe}_3\text{O}_4@\text{SiO}_2@\text{mSiO}_2\text{-NH}_2$ NPs had been modified with Gd-DTPA and RGERPPR-PEG-COOH.

XRD

XRD was employed to confirm the crystal structure of $\text{Fe}_3\text{O}_4@\text{SiO}_2@\text{mSiO}_2$ NPs. The results are given in Figure 2F. The XRD spectrum of Fe_3O_4 NPs showed seven characteristic peaks at 18.75° (111), 30.50° (220), 35.84° (311), 43.46° (400), 53.90° (422), 57.38° (511) and 62.90° (440), which are in good agreement with the standard XRD pattern of Fe_3O_4 (JCPDS No.19-0629). After coating with $\text{SiO}_2@\text{mSiO}_2$, the characteristic peaks of Fe_3O_4 NPs can still be observed, although the intensities were weakened. This result illustrates that the coating of $\text{SiO}_2@\text{mSiO}_2$ did not change the crystal structure of Fe_3O_4 NPs. The hump centered at $2\theta \approx 22^\circ$ is a typical feature of amorphous SiO_2 , suggesting the successful coating of $\text{SiO}_2@\text{mSiO}_2$.

Stability of $\text{Fe}_3\text{O}_4@\text{SiO}_2@\text{mSiO}_2/\text{DOX-(Gd-DTPA)-PEG-RGE}$ NPs

The stability of NPs in serum and normal saline (NS) was assessed by the variation of DLS particle size. The results showed that the NPs could maintain their initial size (ca. 90 ~ 100 nm) in serum (Figure 2G) and NS (Figure S5) over a week, indicating their good stability.

Characterization of RGERPPR-PEG-COOH

The $^1\text{H-NMR}$ spectra of RGERPPR-PEG-COOH and Mal-PEG-COOH are shown in Figure S2A. The $^1\text{H-NMR}$ spectra contain the solvent peak of CDCl_3 at 7.26 ppm, and the peak of repeating units of PEG at 3.7-3.8 ppm. The $^1\text{H-NMR}$ spectrum of Mal-PEG-COOH indicates the presence of the maleimide group by its characteristic peak at 6.7 ppm, whereas that of RGERPPR-PEG-COOH did not show. The results indicated the successful reaction of the thiol group of RGERPPR with the maleimide group.

In Figure S2B, the FTIR spectrum of Mal-PEG-COOH, a weak C=O stretch band at 1658 cm^{-1} and an N-H stretch band at $3200\text{-}3600\text{ cm}^{-1}$ are found, which may be responsible for the amide groups in Mal-PEG-COOH. By comparison, the intensity of the two bands in the spectrum of RGERPPR-PEG-COOH was remarkably enhanced due to the increased number of amide groups from the conjugated RGERPPR peptide. The results indicated that the RGERPPR peptide had been conjugated to Mal-PEG-COOH.

Relaxivity measurements

The T_1 - and T_2 -weighted MR images of $\text{Fe}_3\text{O}_4@\text{SiO}_2@\text{mSiO}_2/\text{DOX-(Gd-DTPA)-PEG-RGE}$ NPs at 3 T MRI were shown in Figure 3. The results showed that as the concentration of NPs increased, T_1 -weighted MR images become brighter, and T_2 -weighted MR images become darker. Meanwhile, 3 T MRI results confirmed that the r_1 relaxivity value of $\text{Fe}_3\text{O}_4@\text{SiO}_2@\text{mSiO}_2/\text{DOX-(Gd-DTPA)-PEG-RGE}$ NPs ($6.13\text{ mM}^{-1}\text{s}^{-1}$) was 1.5 times of that of Magnevist (Gd-DTPA) ($4.02\text{ mM}^{-1}\text{s}^{-1}$) [44]. The r_2 relaxivity value of the NPs was determined to be $36.89\text{ mM}^{-1}\text{s}^{-1}$. The results demonstrated an improved T_1 - T_2 dual mode contrast effect of the NPs. The high r_1 relaxivity may be attributed to the prolongation of the rotational correlation time caused by the restricted local motion, which is similar to the previous reports [48, 49].

DOX loading and pH-responsive release

The DOX molecules can be readily loaded into the mesopore network in the outer silica shell of $\text{Fe}_3\text{O}_4@\text{SiO}_2@\text{mSiO}_2\text{-(Gd-DTPA)-PEG-RGE}$ NPs on account of the large surface area of the mesoporous silica. The DOX loading capacity was determined to be 27.2 wt%, almost similar with that of $\text{Fe}_3\text{O}_4@\text{SiO}_2@\text{mSiO}_2\text{-(Gd-DTPA)-PEG}$ NPs (27.8 wt%). The pH-dependent kinetics of DOX release was verified in pH 7.4, pH 6.5 and pH 5.5 PBS at 37°C for 48 h (Figure S3). DOX release from the two types of NPs was remarkably increased as the pH decreased. At 48 h, the cumulative release rate of DOX from $\text{Fe}_3\text{O}_4@\text{SiO}_2@\text{mSiO}_2/\text{DOX-(Gd-DTPA)-PEG-RGE}$ NPs reached 54.9% at pH 5.5, 36.7% at pH 6.5 and 14.7% at pH 7.4, respectively. Moreover, DOX release from the both types of NPs showed pH sensitivity. This pH-responsive property may be attributed to the protonation of silanol (-Si-OH) on mSiO_2 [50] and amine (-NH₂) in DOX at low pH [51]. Importantly, it can effectively prevent the drug leakage during the blood circulation but facilitate drug release in the mild acidic tumor microenvironment, which would be of significance in tumor treatment.

Cytotoxicity assays

The cell viability of U87MG cells was evaluated following incubation with DOX, $\text{Fe}_3\text{O}_4@SiO_2@mSiO_2/\text{DOX}-(\text{Gd-DTPA})\text{-PEG}$ NPs, and $\text{Fe}_3\text{O}_4@SiO_2@mSiO_2/\text{DOX}-(\text{Gd-DTPA})\text{-PEG-RGE}$ NPs as shown in Figure S4A. The results showed that the cell viability of the three formulations all gradually decreased as the drug concentration increased. Moreover, the $\text{Fe}_3\text{O}_4@SiO_2@mSiO_2/\text{DOX}-(\text{Gd-DTPA})\text{-PEG-RGE}$ NPs showed the highest cytotoxicity compared with DOX and $\text{Fe}_3\text{O}_4@SiO_2@mSiO_2/\text{DOX}-(\text{Gd-DTPA})\text{-PEG}$ NPs, suggesting the *in vitro* targeting ability of RGERPPR peptide. Besides, the $\text{Fe}_3\text{O}_4@SiO_2@mSiO_2/\text{DOX}-(\text{Gd-DTPA})\text{-PEG-RGE}$ NPs entrapped in tumor cells can release DOX, leading to much lowered cell viability, which demonstrates the high effectiveness of the targeted drug delivery. Figure S4B showed that the two types of NPs without DOX loading were basically non-toxic to cells, indicating that the cytotoxicity of DOX-loaded NPs should be caused by the released DOX.

Cellular uptake in vitro

The cellular uptake of NPs by U87MG cell line was studied by using CLSM and flow cytometer. As shown in Figure S6A and Figure S6B, the mean fluorescent intensities of fluorescent cells in $\text{Fe}_3\text{O}_4@SiO_2@mSiO_2/\text{DiO}-(\text{Gd-DTPA})\text{-PEG-RGE}$ NPs

and $\text{Fe}_3\text{O}_4@SiO_2@mSiO_2/\text{DiO}-(\text{Gd-DTPA})\text{-PEG}$ NPs were 70.57 and 27.89, and the percentages for them were 98.91% and 53.57%, respectively. This result indicated that the cellular uptake of the RGE-modified NPs by U87MG cells was significantly increased compared with that of unmodified NPs.

EG00229 is a small molecular inhibitor of NRP-1 [52, 53]. As shown in Figure S6C, the mean fluorescent intensity of the EG00229 plus RGE-modified NPs group of cells for $\text{Fe}_3\text{O}_4@SiO_2@mSiO_2/\text{DiO}-(\text{Gd-DTPA})\text{-PEG-RGE}$ NPs was 41.73, and the percentage was 69.21%. The EG00229 pre-treatment significantly decreased the cellular uptake of RGE-modified NPs. The above data suggested that the active recognition and interaction of RGERPPR with NRP-1 should be responsible for the increased cellular uptake of RGE-modified NPs.

Near infrared fluorescence in vivo imaging

The results of near infrared fluorescence in vivo imaging (Figure 4) showed that there was significantly more distribution of $\text{Fe}_3\text{O}_4@SiO_2@mSiO_2/\text{DiR}-(\text{Gd-DTPA})\text{-PEG-RGE}$ NPs than that of $\text{Fe}_3\text{O}_4@SiO_2@mSiO_2/\text{DiR}-(\text{Gd-DTPA})\text{-PEG}$ NPs in tumor tissue. The $\text{Fe}_3\text{O}_4@SiO_2@mSiO_2/\text{DiR}-(\text{Gd-DTPA})\text{-PEG-RGE}$ NPs began to accumulate in the tumor tissue 2 h post-injection, reached the maximum at 8 h post-injection, and then gradually decreased and almost disappeared at 24 h. However, the $\text{Fe}_3\text{O}_4@SiO_2@mSiO_2/\text{DiR}-(\text{Gd-DTPA})\text{-PEG}$ NPs was almost invisible in the tumor tissue. The pharmacokinetic profile of DiR in the tumor tissue was drawn based on the semi-quantitative ROI analysis of the *in vivo* fluorescent signal per gram of tumor tissue (Figure 4B). The area under curve ($\text{AUC}_{0-48\text{h}}$) of $\text{Fe}_3\text{O}_4@SiO_2@mSiO_2/\text{DiR}-(\text{Gd-DTPA})\text{-PEG-RGE}$ NPs in tumor was significantly increased compared with that of $\text{Fe}_3\text{O}_4@SiO_2@mSiO_2/\text{DiR}-(\text{Gd-DTPA})\text{-PEG}$ NPs. This could be possibly attributed to the active targeting effect of RGERPPR peptide. The near infrared fluorescence imaging on U87MG tumor-bearing mice is shown in Figure S7. The results showed a similar result with that in small tumors.

T₁-T₂ dual mode MR imaging in vivo

To explore the T₁-T₂ dual mode diagnostic application of $\text{Fe}_3\text{O}_4@SiO_2@mSiO_2/\text{DOX}-(\text{Gd-DTPA})\text{-PEG-RGE}$ NPs, the MRI Tra animal imaging was studied on U87MG tumor-bearing mice. As shown in Figure 5, following *i.v.* injection, the $\text{Fe}_3\text{O}_4@SiO_2@mSiO_2/\text{DOX}-(\text{Gd-DTPA})\text{-PEG}$ NPs produced little contrast effect in the tumor tissue. By comparison, after *i.v.*

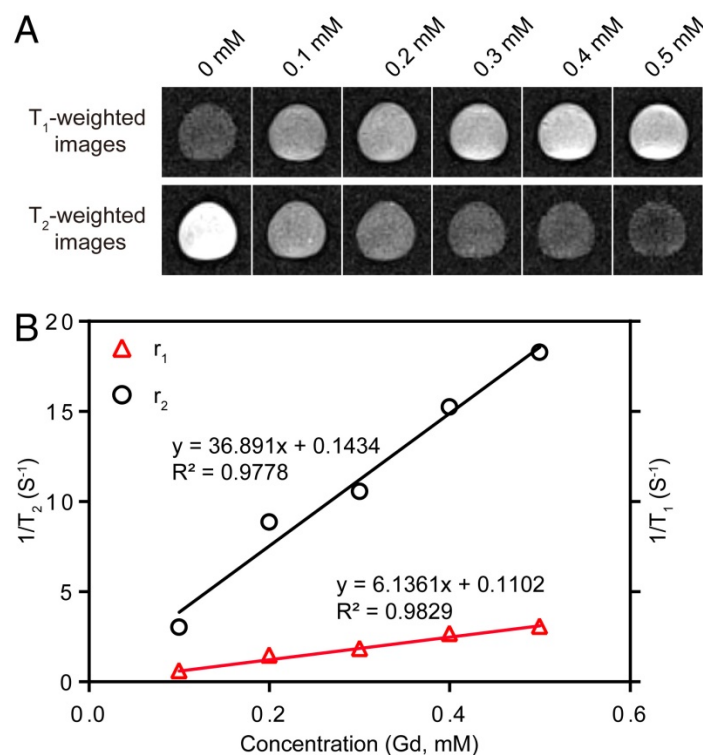


Figure 3. (A) T₁- and T₂-weighted MR images of $\text{Fe}_3\text{O}_4@SiO_2@mSiO_2/\text{DOX}-(\text{Gd-DTPA})\text{-PEG-RGE}$ NPs. (B) T₁ and T₂ relaxivity coefficient of NPs characterized by 3 T MRI.

injection of $\text{Fe}_3\text{O}_4@\text{SiO}_2@m\text{SiO}_2/\text{DOX}-(\text{Gd-DTPA})\text{-PEG-RGE}$ NPs, the T_1 -weighted images of tumor tissue became bright gradually, whereas the T_2 -weighted images became dark. Both T_1 - and T_2 -weighted contrast effect reached the maximum at 8 h post-injection. Compared to the images of pre-injection, the T_1 MR signal ratio of the tumor was increased to 168%, and the T_2 MR signal ratio was decreased to 77.1% (Figure 5B and Figure 5C). These results demonstrated that $\text{Fe}_3\text{O}_4@\text{SiO}_2@m\text{SiO}_2/\text{DOX}-(\text{Gd-DTPA})\text{-PEG-RGE}$ NPs had high r_1 and r_2 relaxivities and exhibited both T_1 -positive and T_2 -negative contrast enhancement on the MR images of tumor simultaneously. The advantage of RGE-modified NPs over unmodified NPs should be attributed to the active targeting effect of tumor-penetrating peptide RGERPPR. The in vitro and in vivo MR results of $\text{Fe}_3\text{O}_4@\text{SiO}_2@m\text{SiO}_2/\text{DOX}-(\text{Gd-DTPA})\text{-PEG-RGE}$ NPs also together demonstrated the advantages of T_1 - T_2 dual mode contrast agents over the single T_1 (Gd-DTPA) and T_2 (Fe_3O_4) contrast agents.

Pharmacokinetic study

The pharmacokinetic study of $\text{Fe}_3\text{O}_4@\text{SiO}_2@m\text{SiO}_2/\text{DiR}-(\text{Gd-DTPA})\text{-PEG}$ NPs and $\text{Fe}_3\text{O}_4@\text{SiO}_2@m\text{SiO}_2/\text{DiR}-(\text{Gd-DTPA})\text{-PEG-RGE}$ NPs was performed to study the systemic circulation time of the NPs in SD rats. The pharmacokinetic curves were shown in Figure 6A, and the pharmacokinetic parameters were calculated and summarized in Table 1. The results showed that the elimination of $\text{Fe}_3\text{O}_4@\text{SiO}_2@m\text{SiO}_2/\text{DiR}-(\text{Gd-DTPA})\text{-PEG-RGE}$ NPs from blood is significantly slower than $\text{Fe}_3\text{O}_4@\text{SiO}_2@m\text{SiO}_2/\text{DiR}-(\text{Gd-DTPA})\text{-PEG}$ NPs. The plasma half-lives of $\text{Fe}_3\text{O}_4@\text{SiO}_2@m\text{SiO}_2/\text{DiR}-(\text{Gd-DTPA})\text{-PEG}$ NPs and $\text{Fe}_3\text{O}_4@\text{SiO}_2@m\text{SiO}_2/\text{DiR}-(\text{Gd-DTPA})\text{-PEG-RGE}$ NPs were 7.39 hours and 10.69 hours, mean residence time (MRT) were 8.35 hours and 11.62 hours, $\text{AUC}_{0-\infty}$ were 17.40 and 33.43, respectively. The RGE-modified NPs showed significantly prolonged circulation time in blood compared with the unmodified NPs. We speculated that it could be attributed to the dynamic equilibrium of the NPs between the blood and the tumor tissue, since the RGE-modified NPs showed significantly increased tumor accumulation and penetration by the mediation of RGERPPR (Figure 6B, Figure 4 and Figure 8).

Bio-distribution study

The tissue bio-distribution of NPs were evaluated in U87MG tumor-bearing mice. As shown in Figure 6B, compared with unmodified NPs, the RGE-modified NPs showed significantly enhanced

accumulation in tumor tissue, which should also be attributed to the tumor penetrating ability of RGERPPR peptide. Both the $\text{Fe}_3\text{O}_4@\text{SiO}_2@m\text{SiO}_2/\text{DiR}-(\text{Gd-DTPA})\text{-PEG}$ NPs and $\text{Fe}_3\text{O}_4@\text{SiO}_2@m\text{SiO}_2/\text{DiR}-(\text{Gd-DTPA})\text{-PEG-RGE}$ NPs showed (Figure 6B) almost no distribution in heart and lung, obvious distribution in liver, and a little distribution in spleen and kidney. The distribution in liver and spleen should be caused by the macrophage phagocytosis of NPs, which is a common feature of nano drug delivery systems [54-57]. The distribution in kidney should be attributed to the elimination of DiR in kidney. The results are almost consistent with that of the in vivo near infrared fluorescence imaging study (Figure 4) and MR imaging study (Figure 5).

Table 1. Pharmacokinetic parameters of $\text{Fe}_3\text{O}_4@\text{SiO}_2@m\text{SiO}_2/\text{DiR}-(\text{Gd-DTPA})\text{-PEG}$ NPs and $\text{Fe}_3\text{O}_4@\text{SiO}_2@m\text{SiO}_2/\text{DiR}-(\text{Gd-DTPA})\text{-PEG-RGE}$ NPs.

Parameter	$\text{Fe}_3\text{O}_4@\text{SiO}_2@m\text{SiO}_2/\text{DiR}-(\text{Gd-DTPA})\text{-PEG}$ NPs	$\text{Fe}_3\text{O}_4@\text{SiO}_2@m\text{SiO}_2/\text{DiR}-(\text{Gd-DTPA})\text{-PEG-RGE}$ NPs
$t_{1/2}$ (h)	7.39 ± 2.49	10.69 ± 2.75
MRT (h)	8.35 ± 1.18	11.62 ± 2.89
$\text{AUC}_{0-\infty}$ ($\mu\text{g/g h}$)	17.40 ± 1.83	33.43 ± 4.77

Data are represented with mean ± SD (n = 3).

The antitumor effect in vivo

The in vivo antitumor efficacy of $\text{Fe}_3\text{O}_4@\text{SiO}_2@m\text{SiO}_2/\text{DOX}-(\text{Gd-DTPA})\text{-PEG-RGE}$ NPs was investigated on the U87MG tumor-bearing mice. As shown in Figure 6C, $\text{Fe}_3\text{O}_4@\text{SiO}_2@m\text{SiO}_2/\text{DOX}-(\text{Gd-DTPA})\text{-PEG-RGE}$ NPs significantly inhibited the tumor growth, whereas DOX and $\text{Fe}_3\text{O}_4@\text{SiO}_2@m\text{SiO}_2/\text{DOX}-(\text{Gd-DTPA})\text{-PEG}$ NPs showed much weaker tumor inhibition effect ($P < 0.001$). Such an enhanced tumor-inhibition effect of $\text{Fe}_3\text{O}_4@\text{SiO}_2@m\text{SiO}_2/\text{DOX}-(\text{Gd-DTPA})\text{-PEG-RGE}$ NPs could be explained by the increased accumulation of the NPs within tumor due to the mediation of RGERPPR peptide, and the pH sensitive DOX release from the NPs in the mild acidic tumor microenvironment. In addition, the mice in $\text{Fe}_3\text{O}_4@\text{SiO}_2@m\text{SiO}_2/\text{DOX}-(\text{Gd-DTPA})\text{-PEG-RGE}$ NPs group showed the most increased mean body weight during the experiment compared with other groups (Figure 6D), which probably resulted from the good physical condition of mice due to the tumor suppression.

Histology verification

The antitumor effect of $\text{Fe}_3\text{O}_4@\text{SiO}_2@m\text{SiO}_2/\text{DOX}-(\text{Gd-DTPA})\text{-PEG-RGE}$ NPs in vivo was further evaluated by the H&E staining and TUNEL assay.

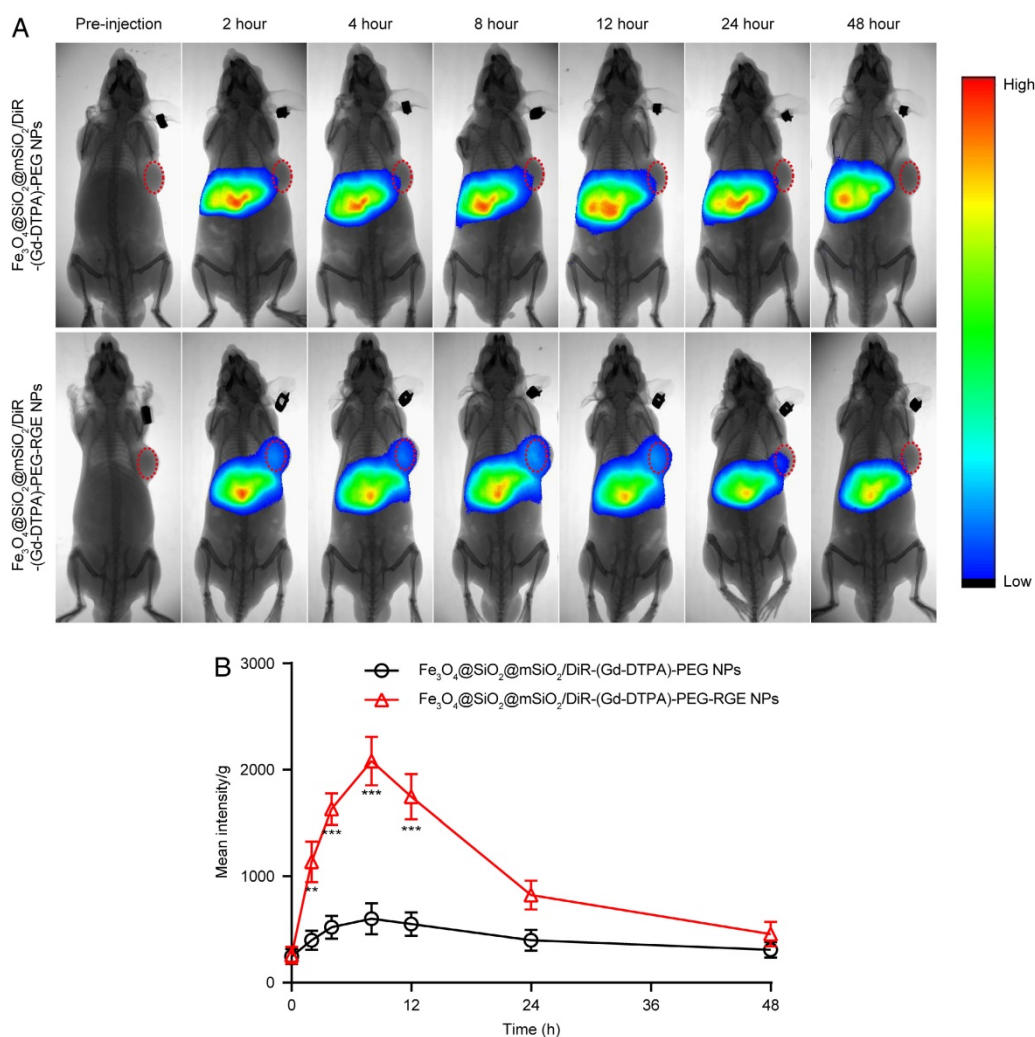


Figure 4. (A) In vivo fluorescent imaging of $\text{Fe}_3\text{O}_4@(\text{SiO}_2@m\text{SiO}_2/\text{DiR}-(\text{Gd-DTPA))\text{-PEG NPs}$ and $\text{Fe}_3\text{O}_4@(\text{SiO}_2@m\text{SiO}_2/\text{DiR}-(\text{Gd-DTPA))\text{-PEG-RGE NPs}$ on small U87MG tumor-bearing mice ($n = 3$) following i.v. administration of NPs at different time points. Color bar on the right side indicates the signal intensity of the fluorescence. (B) The pharmacokinetic profile of DiR in tumor tissue based on the semi-quantitative ROI analysis of in vivo fluorescent images.

H&E staining

The H&E staining assay was performed to evaluate the antitumor effect of $\text{Fe}_3\text{O}_4@(\text{SiO}_2@m\text{SiO}_2/\text{DOX}-(\text{Gd-DTPA))\text{-PEG-RGE NPs}$ by the slides of tumor tissue and the histocompatibility by the slides of main organs. The tumor tissue slides of the $\text{Fe}_3\text{O}_4@(\text{SiO}_2@m\text{SiO}_2/\text{DOX}-(\text{Gd-DTPA))\text{-PEG-RGE NPs}$ group showed the strongest necrosis of tumor cells compared with the other three groups (Figure 7, the red arrow). In contrast, the main organs (including heart, liver, spleen, lung, and kidney) of the $\text{Fe}_3\text{O}_4@(\text{SiO}_2@m\text{SiO}_2/\text{DOX}-(\text{Gd-DTPA))\text{-PEG-RGE NPs}$ group showed almost no obvious pathological abnormality compared with Saline group (Figure S8), indicating a good histocompatibility of the NPs. Importantly, the NPs resulted in a decreased toxicity to normal organs compared with DOX, which could cause significant damage to liver, heart, kidney, and spleen, as clearly demonstrated by the H&E staining

results (Figure S8). The above results of H&E staining are also consistent with the in vivo antitumor results.

TUNEL assay

As shown in Figure 7, the tumor tissue slides of the $\text{Fe}_3\text{O}_4@(\text{SiO}_2@m\text{SiO}_2/\text{DOX}-(\text{Gd-DTPA))\text{-PEG-RGE NPs}$ group displayed much more TUNEL-positive cells compared with the other three groups (Figure 7, the red arrow). The results indicated that RGE modification could significantly enhance the antitumor effect of the DOX-loaded NPs, thereby causing increased apoptosis of tumor cells. The TUNEL assay results are basically consistent with the above in vivo antitumor results (Figure 6).

Tumor-penetrating ability of $\text{Fe}_3\text{O}_4@(\text{SiO}_2@m\text{SiO}_2/\text{DiO}-(\text{Gd-DTPA))\text{-PEG-RGE NPs}$

The tumor-penetrating ability of $\text{Fe}_3\text{O}_4@(\text{SiO}_2@m\text{SiO}_2/\text{DiO}-(\text{Gd-DTPA))\text{-PEG-RGE NPs}$ in U87MG

tumor-bearing mice was investigated by the immunofluorescence analysis of frozen sections. The immunofluorescence images (Figure 8) showed that the i.v. injected $\text{Fe}_3\text{O}_4@SiO_2@mSiO_2/DiO-(Gd-DTPA)-PEG$ NPs were thinly distributed in the tumor tissue, whereas $\text{Fe}_3\text{O}_4@SiO_2@mSiO_2/DiO-(Gd-DTPA)-PEG-RGE$ NPs were located in the whole tumor tissue (green fluorescence). The results suggested that RGERPPR modification enabled NPs to penetrate through tumor vessels and tumor stroma and deep into the whole tumor tissue. The $\text{Fe}_3\text{O}_4@SiO_2@mSiO_2/DiO-(Gd-DTPA)-PEG-RGE$ NPs showed (Figure S9) similar bio-distribution in vivo with $\text{Fe}_3\text{O}_4@SiO_2@mSiO_2/DiR-(Gd-DTPA)-PEG-RGE$ NPs showed (Figure 6B).

Discussion

In this work, we prepared a tumor-penetrating peptide RGE modified, Gd-DTPA conjugated, and DOX-loaded $\text{Fe}_3\text{O}_4@SiO_2@mSiO_2$ nanoparticle drug delivery system ($\text{Fe}_3\text{O}_4@SiO_2@mSiO_2/DOX-(Gd-DTPA)-PEG-RGE$ NPs) for tumor theranostics. The NPs showed a pH-sensitive DOX release profile and a T_1 - T_2 dual mode contrast effect in vitro. The modification of RGERPPE peptide significantly increased the cellular uptake, cytotoxicity, tumor accumulation, T_1 - T_2 dual mode contrast imaging effect at tumor tissue, tumor penetrating ability, and the antitumor effect of the NPs.

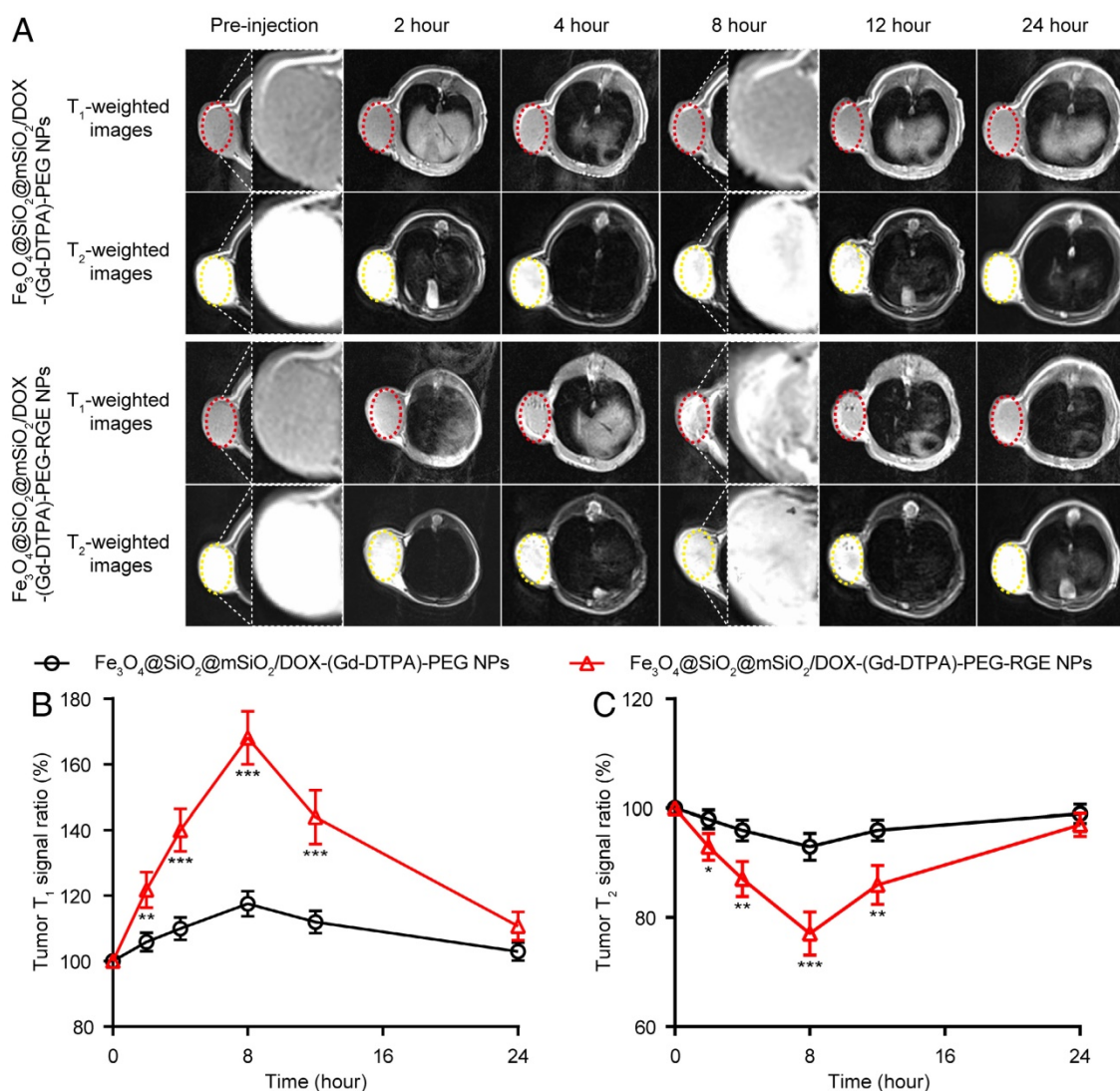


Figure 5. T_1 - T_2 dual mode MR imaging of U87MG tumor-bearing mice ($n = 3$) with $\text{Fe}_3\text{O}_4@SiO_2@mSiO_2/DOX-(Gd-DTPA)-PEG-RGE$ NPs in vivo. (A) Representative in vivo T_1 - and T_2 -weighted MR images of mice following i.v. administration of $\text{Fe}_3\text{O}_4@SiO_2@mSiO_2/DOX-(Gd-DTPA)-PEG$ NPs and $\text{Fe}_3\text{O}_4@SiO_2@mSiO_2/DOX-(Gd-DTPA)-PEG-RGE$ NPs at different time points. (B, C) Quantitative analysis of T_1 - and T_2 -weighted MR images tumor contrast enhancement after i.v. injection of $\text{Fe}_3\text{O}_4@SiO_2@mSiO_2/DOX-(Gd-DTPA)-PEG$ NPs and $\text{Fe}_3\text{O}_4@SiO_2@mSiO_2/DOX-(Gd-DTPA)-PEG-RGE$ NPs. The average MR relative T_1 and T_2 signal enhancements were measured for each tumor. The higher contrast of tumor positions by $\text{Fe}_3\text{O}_4@SiO_2@mSiO_2/DOX-(Gd-DTPA)-PEG-RGE$ NPs may result from the active targeting effect of tumor-penetrating peptide RGERPPR.

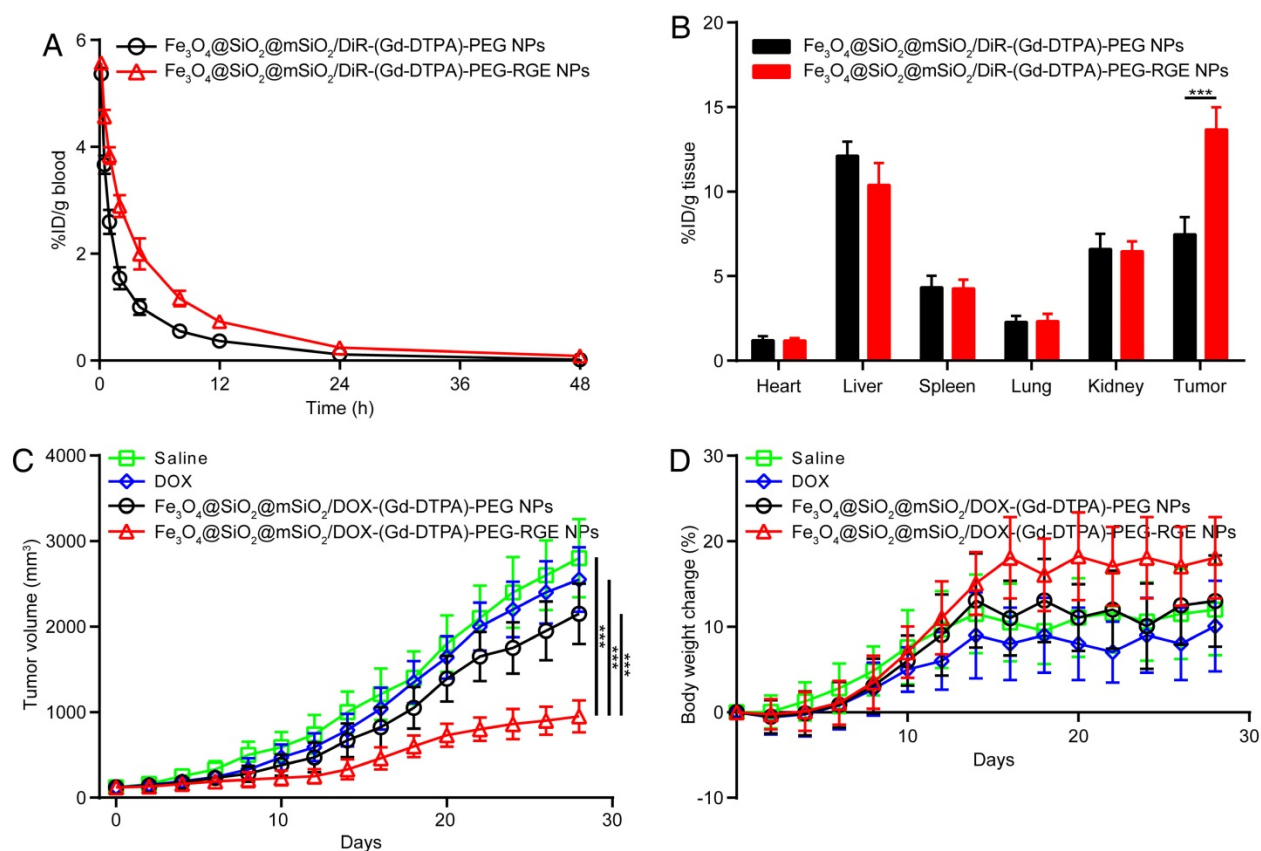


Figure 6. The pharmacokinetic curves of the NPs on SD rats (A); The bio-distribution (B) and antitumor efficacy of the NPs on U87MG tumor-bearing mice. Tumor growth curves (C), Body weight change (D). RGE-modified NPs showed significantly increased MRT, tumor distribution, and antitumor efficacy compared with unmodified NPs.

The active tumor-targeted nano-drug delivery system is generally comprised of the drug-loaded carrier (such as liposomes, micelles, polymeric nanoparticles, polymer-drug conjugates) and the modified targeting molecules on the surface that can actively recognize the specific receptor overexpressed on tumor cells. Although the active targeting drug delivery systems have been extensively studied, their therapeutic effects have not been significantly improved as expected compared with the unmodified drug delivery systems. There may be many reasons for this issue, but many researchers believed that the heterogeneity of the EPR effect and the limitation of the targeting molecules should be primarily responsible for this. For one thing, the EPR effect is heterogeneous, which depends on the tumor type, the body condition of the patients, the site of the tumor, etc. This would affect the tumor accumulation of nano-drug delivery system, and ultimately the treatment effect. For another, the active recognition of tumor cells should have a prerequisite that the drug delivery system enters the tumor tissue and penetrates into the deep tumor tissue to be close to the

tumor cells. However, most of the targeting molecules currently used in the active targeting drug delivery system only bind to the receptors expressed on the tumor cells, and the modification of the targeting molecules does not help the nano-drug delivery system enter and penetrate the tumor tissue. Accordingly, tumor-penetrating peptides (TPPs) should be the ideal targeting molecules for the tumor-targeted drug delivery system. This is because that the receptor of TPPs, NRP-1, is distributed both on tumor cells and tumor blood vessels, and more importantly that the TPPs can penetrate through the tumor vessel wall and tumor stroma [30-32]. The penetration through the tumor vessel wall can break the limitation of the EPR effect, so that the nano-drug delivery system can enter tumor tissue by virtue of not only the EPR effect, but also the penetrating ability of the TPPs. Besides, the penetration through the tumor stroma can help the nano-drug delivery system be transported to the entire tumor tissue. These abilities of tumor-penetrating peptides have been well demonstrated by the above results (Figure S6, Figure 4 and Figure 8).

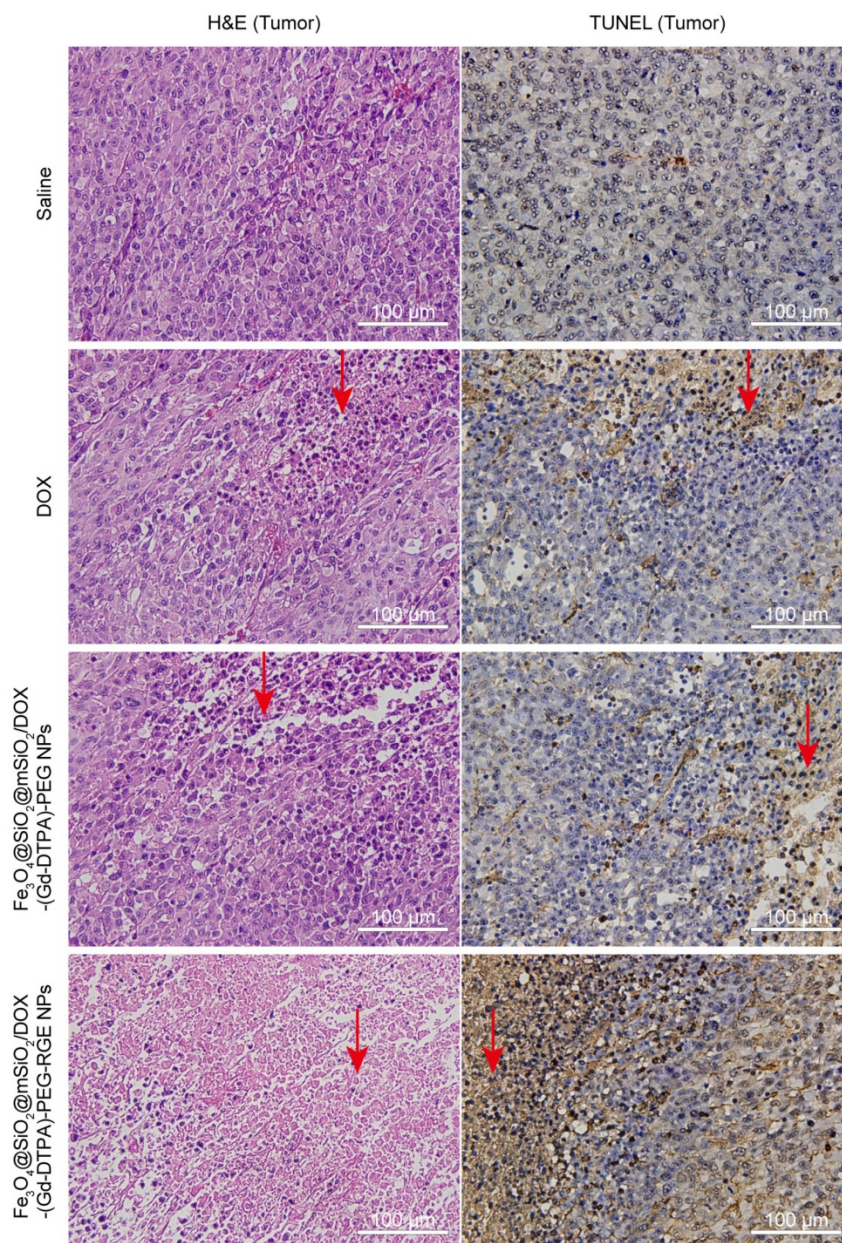


Figure 7. The H&E staining and TUNEL slides of tumor tissues harvested from U87MG tumor-bearing mice ($n = 3$) after the treatment with Saline (control), DOX, $\text{Fe}_3\text{O}_4@SiO_2@mSiO_2/DOX-(Gd-DTPA)-PEG$ NPs, and $\text{Fe}_3\text{O}_4@SiO_2@mSiO_2/DOX-(Gd-DTPA)-PEG-RGE$ NPs ($40\times$). The tumor tissue slides of the $\text{Fe}_3\text{O}_4@SiO_2@mSiO_2/DOX-(Gd-DTPA)-PEG-RGE$ NPs group showed a large amount of cell death (H&E staining) and significant apoptosis (TUNEL assay) compared with the Saline group, DOX group, and $\text{Fe}_3\text{O}_4@SiO_2@mSiO_2/DOX-(Gd-DTPA)-PEG$ NPs group (the red arrow).

The enough stability in vivo and timely drug release in tumor tissue are both important for the TDDS. Too stabilized TDDS often results in the insufficient drug release at the tumor site, whereas poorly stabilized TDDS may lead to the drug leakage during the blood circulation, causing low accumulation in tumor tissue and side effects to normal tissues. Thus, it is highly desirable for the TDDS to find a balance between the enough stability in vivo and timely drug release in tumor tissue [58]. In this study, the NPs we prepared showed sufficient stability in serum (Figure 2G) and pH-sensitive drug release (Figure S3), which are beneficial for long

circulation in blood and timely drug release in tumor tissue or tumor cells. The pH-sensitive drug release of DOX from the $mSiO_2$ NPs may be attributed to the protonation of silanol ($-Si-OH$) on $mSiO_2$ [50] and amine ($-NH_2$) in DOX at low pH [51]. The protonation of amine increases the water solubility of DOX. Besides, the protonation makes both $mSiO_2$ and DOX positively charged. The electrostatic repulsion between them further increased the DOX release. By contrast, in the physiological condition ($pH = 7.4$), the uncharged DOX may easily be adsorbed by $mSiO_2$ and cannot be adequately released.

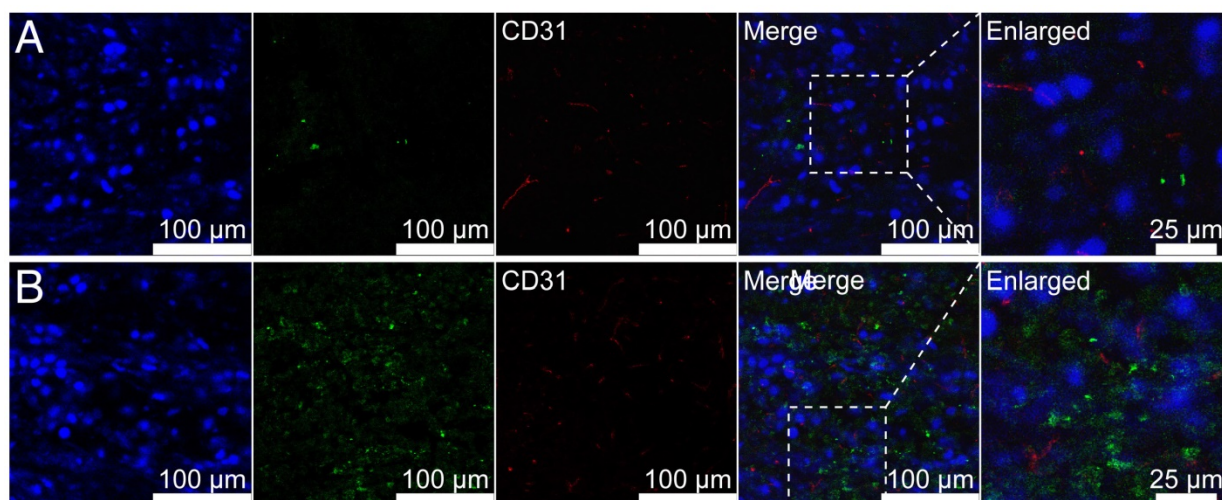


Figure 8. Representative immunofluorescence images of frozen U87MG tumor-bearing mice ($n = 3$) following injection of $\text{Fe}_3\text{O}_4@SiO_2@mSiO_2/DiO-(Gd-DTPA)-PEG$ NPs (A) and $\text{Fe}_3\text{O}_4@SiO_2@mSiO_2/DiO-(Gd-DTPA)-PEG-RGE$ NPs (B). $\text{Fe}_3\text{O}_4@SiO_2@mSiO_2/DiO-(Gd-DTPA)-PEG$ NPs were thinly distributed in the tumor tissue, whereas $\text{Fe}_3\text{O}_4@SiO_2@mSiO_2/DiO-(Gd-DTPA)-PEG-RGE$ NPs penetrated through tumor vessels and tumor stroma and deep into the whole tumor tissue.

In summary, we successfully developed $\text{Fe}_3\text{O}_4@SiO_2@mSiO_2/DOX-(Gd-DTPA)-PEG-RGE$ NPs for tumor theranostics. The NPs showed the integrated function of T_1 - T_2 dual mode MR imaging effect, pH-sensitivity of DOX release and tumor-penetrating ability. The RGERPPR peptide modification played an important role in enhancing the effect of tumor therapeutics and MR imaging. The multifunctional NPs may be traced in vivo in real time, and provide timely feedback on the clinical effectiveness of the loaded drug. This study proved that the NPs are an effective drug delivery system for tumor theranostics, and should have a potential value in the personalized treatment of tumor.

Abbreviations

MRI: magnetic resonance imaging; TDDS: tumor targeted drug delivery systems; NRP-1: Neuropilin-1; EPR: enhanced permeation and retention; DOX: doxorubicin; DLS: dynamic light scattering; TEM: transmission electron microscopy; CLSM: confocal laser scanning microscope; CCK-8: Cell Counting Kit-8; DiO: 3,3'-dioctadecyloxycarbocyanine, perchlorate; DiR: 1,1'-dioctadecyl-3,3',3'-tetramethyl indotricarbocyanine Iodide; DMEM: Dulbecco's Modified Eagle Medium; FBS: fetal bovine serum; PBS: phosphate buffer solution; NS: normal saline; AUC: area under curve; H&E: Hematoxylin and Eosin; TUNEL: TdT-mediated dUTP Nick-End Labeling; IACUC: Institutional Animal Care and Use Committee.

Acknowledgments

This work was supported by National Basic Research Program of China (2013CB932500, 2014CB744505), National Natural Science Foundation of China (60976004, 81430040, 81571738), "985" grants of East China Normal University (ECNU).

Supplementary Material

Supplementary figures.

<http://www.thno.org/v08p0092s1.pdf>

Competing Interests

The authors have declared that no competing interest exists.

References

1. Siegel RL, Miller KD, Jemal A. Cancer Statistics, 2017. *CA Cancer J Clin.* 2017; 67: 7-30.
2. Kumar R, Shin WS, Sunwoo K, Kim WY, Koo S, Bhuniya S, et al. Small conjugate-based theranostic agents: an encouraging approach for cancer therapy. *Chem Soc Rev.* 2015; 44: 6670-83.
3. Wang S, Huang P, Chen X. Stimuli-Responsive Programmed Specific Targeting in Nanomedicine. *ACS Nano.* 2016; 10: 2991-4.
4. Wang S, Lin J, Wang T, Chen X, Huang P. Recent Advances in Photoacoustic Imaging for Deep-Tissue Biomedical Applications. *Theranostics.* 2016; 6: 2394-413.
5. Wang Y, Chen J, Yang B, Qiao H, Gao L, Su T, et al. In vivo MR and Fluorescence Dual-modality Imaging of Atherosclerosis Characteristics in Mice Using Profilin-1 Targeted Magnetic Nanoparticles. *Theranostics.* 2016; 6: 272-86.
6. Chandrasekharan P, Maity D, Yong CX, Chuang KH, Ding J, Feng SS. Vitamin E (D-alpha-tocopheryl-co-poly(ethylene glycol) 1000 succinate) micelles-superparamagnetic iron oxide nanoparticles for enhanced radiotherapy and MRI. *Biomaterials.* 2011; 32: 5663-72.
7. Gao L, Zhou J, Yu J, Li Q, Liu X, Sun L, et al. A Novel Gd-DTPA-conjugated Poly(L-glytutamyl-glutamine)-paclitaxel Polymeric Delivery System for Tumor Theranostics. *Sci Rep.* 2017; 7: 3799.
8. Muthu MS, Kulkarni SA, Raju A, Feng SS. Theranostic liposomes of TPGS coating for targeted co-delivery of docetaxel and quantum dots. *Biomaterials.* 2012; 33: 3494-501.
9. Wang X, Tang H, Wang C, Zhang J, Wu W, Jiang X. Phenylboronic Acid-Mediated Tumor Targeting of Chitosan Nanoparticles. *Theranostics.* 2016; 6: 1378-92.

10. Muthu MS, Leong DT, Mei L, Feng SS. Nanotheranostics - application and further development of nanomedicine strategies for advanced theranostics. *Theranostics*. 2014; 4: 660-77.
11. Robinson JT, Welsher K, Tabakman SM, Sherlock SP, Wang H, Luong R, et al. High Performance In Vivo Near-IR (>1 μm) Imaging and Photothermal Cancer Therapy with Carbon Nanotubes. *Nano research*. 2010; 3: 779-93.
12. Wang H, Tang L, Liu Y, Dobrucka IT, Dobrucki LW, Yin L, et al. In Vivo Targeting of Metabolically Labeled Cancers with Ultra-Small Silica Nanoconjugates. *Theranostics*. 2016; 6: 1467-76.
13. Tong X, Wang Z, Sun X, Song J, Jacobson O, Niu G, et al. Size Dependent Kinetics of Gold Nanorods in EPR Mediated Tumor Delivery. *Theranostics*. 2016; 6: 2039-51.
14. Yu L, Chen Y, Wu M, Cai X, Yao H, Zhang L, et al. "Manganese Extraction" Strategy Enables Tumor-Sensitive Biodegradability and Theranostics of Nanoparticles. *J Am Chem Soc*. 2016; 138: 9881-94.
15. Pan L, He Q, Liu J, Chen Y, Ma M, Zhang L, et al. Nuclear-targeted drug delivery of TAT peptide-conjugated monodisperse mesoporous silica nanoparticles. *J Am Chem Soc*. 2012; 134: 5722-5.
16. Li X, Zhao W, Liu X, Chen K, Zhu S, Shi P, et al. Mesoporous manganese silicate coated silica nanoparticles as multi-stimuli-responsive T1-MRI contrast agents and drug delivery carriers. *Acta Biomater*. 2016; 30: 378-87.
17. Zhang K, Liu M, Tong X, Sun N, Zhou L, Cao Y, et al. Aptamer-Modified Temperature-Sensitive Liposomal Contrast Agent for Magnetic Resonance Imaging. *Biomacromolecules*. 2015; 16: 2618-23.
18. Zu G, Liu M, Zhang K, Hong S, Dong J, Cao Y, et al. Functional Hyperbranched Polylysine as Potential Contrast Agent Probes for Magnetic Resonance Imaging. *Biomacromolecules*. 2016; 17: 2302-8.
19. Verwilst P, Park S, Yoon B, Kim JS. Recent advances in Gd-chelate based bimodal optical/MRI contrast agents. *Chem Soc Rev*. 2015; 44: 1791-806.
20. Jackson AW, Chandrasekharan P, Ramasamy B, Goggi J, Chuang KH, He T, et al. Octreotide Functionalized Nano-Contrast Agent for Targeted Magnetic Resonance Imaging. *Biomacromolecules*. 2016; 17: 3902-10.
21. Jaidev LR, Chellappan DR, Bhavsar DV, Ranganathan R, Sivanantham B, Subramanian A, et al. Multi-functional nanoparticles as theranostic agents for the treatment & imaging of pancreatic cancer. *Acta Biomater*. 2017; 49: 422-33.
22. Ren L, Chen S, Li H, Zhang Z, Zhong J, Liu M, et al. MRI-guided liposomes for targeted tandem chemotherapy and therapeutic response prediction. *Acta Biomater*. 2016; 35: 260-8.
23. Padmanabhan P, Kumar A, Kumar S, Chaudhary RK, Gulyas B. Nanoparticles in practice for molecular-imaging applications: An overview. *Acta Biomater*. 2016; 41: 1-16.
24. Liu XL, Ng CT, Chandrasekharan P, Yang HT, Zhao LY, Peng E, et al. Synthesis of Ferromagnetic Fe_{0.6}Mn_{0.4}O Nanoflowers as a New Class of Magnetic Theranostic Platform for In Vivo T1-T2 Dual-Mode Magnetic Resonance Imaging and Magnetic Hyperthermia Therapy. *Advanced healthcare materials*. 2016; 5: 2092-104.
25. Shin T, Choi J, Yun S, Kim I, Song H, Kim Y, et al. T₁ and T₂ dual-mode MRI contrast agent for enhancing accuracy by engineered nanomaterials. *ACS Nano*. 2014; 8: 3393-401.
26. Yang H, Zhuang Y, Sun Y, Dai A, Shi X, Wu D, et al. Targeted dual-contrast T₁- and T₂-weighted magnetic resonance imaging of tumors using multifunctional gadolinium-labeled superparamagnetic iron oxide nanoparticles. *Biomaterials*. 2011; 32: 4584-93.
27. Kamaly N, Xiao Z, Valencia PM, Radovic-Moreno AF, Farokhzad OC. Targeted polymeric therapeutic nanoparticles: design, development and clinical translation. *Chem Soc Rev*. 2012; 41: 2971-3010.
28. Wang X, Li S, Shi Y, Chuan X, Li J, Zhong T, et al. The development of site-specific drug delivery nanocarriers based on receptor mediation. *J Control Release*. 2014; 193: 139-53.
29. Ying M, Shen Q, Liu Y, Yan Z, Wei X, Zhan C, et al. Stabilized Heptapeptide A7R for Enhanced Multifunctional Liposome-Based Tumor-Targeted Drug Delivery. *ACS Appl Mater Interfaces*. 2016; 8: 13232-41.
30. Teesalu T, Sugahara KN, Kotamraju VR, Ruoslahti E. C-end rule peptides mediate neuropilin-1-dependent cell, vascular, and tissue penetration. *Proc Natl Acad Sci U S A*. 2009; 106: 16157-62.
31. Simon-Gracia L, Hunt H, Scodeller P, Gaitzsch J, Kotamraju VR, Sugahara KN, et al. iRGD peptide conjugation potentiates intraperitoneal tumor delivery of paclitaxel with polymersomes. *Biomaterials*. 2016; 104: 247-57.
32. Braun GB, Sugahara KN, Yu OM, Kotamraju VR, Molder T, Lowy AM, et al. Urokinase-controlled tumor penetrating peptide. *J Control Release*. 2016; 232: 188-95.
33. Wang J, Lei Y, Xie C, Lu W, Yan Z, Gao J, et al. Targeted gene delivery to glioblastoma using a C-end rule RGERPPR peptide-functionalised polyethylenimine complex. *Int J Pharm*. 2013; 458: 48-56.
34. Yang Y, Yan Z, Wei D, Zhong J, Liu L, Zhang L, et al. Tumor-penetrating peptide functionalization enhances the anti-glioblastoma effect of doxorubicin liposomes. *Nanotechnology*. 2013; 24: 405101.
35. Park J, An K, Hwang Y, Park JG, Noh HJ, Kim JY, et al. Ultra-large-scale syntheses of monodisperse nanocrystals. *Nat Mater*. 2004; 3: 891-5.
36. Lee DC, Mikulec FV, Pelaez JM, Koo B, Korgel BA. Synthesis and Magnetic Properties of Silica-Coated FePt Nanocrystals. *J Phys Chem B*. 2006; 110: 11160-6.
37. Chen F, Bu W, Chen Y, Fan Y, He Q, Zhu M, et al. A sub-50-nm monosized superparamagnetic Fe₃O₄/SiO₂ T₂-weighted MRI contrast agent: highly reproducible synthesis of uniform single-loaded core-shell nanostructures. *Chem Asian J*. 2009; 4: 1809-16.
38. Liu J, Liu Y, Bu W, Bu J, Sun Y, Du J, et al. Ultrasensitive Nanosensors Based on Upconversion Nanoparticles for Selective Hypoxia Imaging in Vivo upon Near-Infrared Excitation. *Journal of the American Chemical Society*. 2014; 136: 9701-9.
39. Hu Q, Gu G, Liu Z, Jiang M, Kang T, Miao D, et al. F3 peptide-functionalized PEG-PLA nanoparticles co-administrated with tlyp-1 peptide for anti-glioma drug delivery. *Biomaterials*. 2013; 34: 1135-45.
40. Shin TH, Choi Y, Kim S, Cheon J. Recent advances in magnetic nanoparticle-based multi-modal imaging. *Chem Soc Rev*. 2015; 44: 4501-16.
41. Song Y, Guan R, Lyu F, Kang T, Wu Y, Chen X. In vitro cytotoxicity of silver nanoparticles and zinc oxide nanoparticles to human epithelial colorectal adenocarcinoma (Caco-2) cells. *Mutat Res*. 2014; 769: 113-8.
42. Chang B, Guo J, Liu C, Qian J, Yang W. Surface functionalization of magnetic mesoporous silica nanoparticles for controlled drug release. *Journal of Materials Chemistry*. 2010; 20: 9941.
43. Negishi T, Koizumi F, Uchino H, Kuroda J, Kawaguchi T, Naito S, et al. NK105, a paclitaxel-incorporating micellar nanoparticle, is a more potent radiosensitizing agent compared to free paclitaxel. *Br J Cancer*. 2006; 95: 601-6.
44. Cai J, Gu B, Cao F, Liu S. A transferrin-target magnetic/fluorescent dual-mode probe significantly enhances the diagnosis of non-small cell lung cancer. *Oncotarget*. 2016; 7: 40047-59.
45. Kitamoto K, Machida Y, Uchida J, Izumi Y, Shiota M, Nakao T, et al. Effects of liposome clodronate on renal leukocyte populations and renal fibrosis in murine obstructive nephropathy. *J Pharmacol Sci*. 2009; 111: 285-92.
46. Yang D, Van S, Shu Y, Liu X, Ge Y, Jiang X, et al. Synthesis, characterization, and in vivo efficacy evaluation of PGC-docetaxel conjugate for potential cancer chemotherapy. *Int J Nanomedicine*. 2012; 7: 581-9.
47. Yoon TJ, Yu KN, Kim E, Kim JS, Kim BG, Yun SH, et al. Specific targeting, cell sorting, and bioimaging with smart magnetic silica core-shell nanomaterials. *Small*. 2006; 2: 209-15.
48. Huang YR, He S, Cao WP, Cai KY, Liang XJ. Biomedical nanomaterials for imaging-guided cancer therapy. *Nanoscale*. 2012; 4: 6135-49.
49. Mi P, Cabral H, Kokuryo D, Rafi M, Terada Y, Aoki I, et al. Gd-DTPA-loaded polymer-metal complex micelles with high relaxivity for MR cancer imaging. *Biomaterials*. 2013; 34: 492-500.
50. Ma M, Chen H, Chen Y, Wang X, Chen F, Cui X, et al. Au capped magnetic core/mesoporous silica shell nanoparticles for combined photothermo-/chemo-therapy and multimodal imaging. *Biomaterials*. 2012; 33: 989-98.
51. Yang G, Gong H, Liu T, Sun X, Cheng L, Liu Z. Two-dimensional magnetic WS₂@Fe₃O₄ nanocomposite with mesoporous silica coating for drug delivery and imaging-guided therapy of cancer. *Biomaterials*. 2015; 60: 62-71.
52. Jarvis A, Allerston CK, Jia H, Herzog B, Garza-Garcia A, Winfield N, et al. Small molecule inhibitors of the neuropilin-1 vascular endothelial growth factor A (VEGF-A) interaction. *Journal of medicinal chemistry*. 2010; 53: 2215-26.
53. Grun D, Adhikary G, Eckert RL. VEGF-A acts via neuropilin-1 to enhance epidermal cancer stem cell survival and formation of aggressive and highly vascularized tumors. *Oncogene*. 2016; 35: 4379-87.
54. Walkey CD, Olsen JB, Guo H, Emili A, Chan WC. Nanoparticle size and surface chemistry determine serum protein adsorption and macrophage uptake. *J Am Chem Soc*. 2012; 134: 2139-47.
55. Evensen L, Johansen PL, Koster G, Zhu K, Herfindal L, Speth M, et al. Zebrafish as a model system for characterization of nanoparticles against cancer. *Nanoscale*. 2016; 8: 862-77.
56. Vene E, Barouti G, Jarnouen K, Gicquel T, Rauch C, Ribault C, et al. Opsonisation of nanoparticles prepared from poly(beta-hydroxybutyrate) and poly(trimethylene carbonate)-b-poly(malic acid) amphiphilic diblock copolymers: Impact on the in vitro cell uptake by primary human macrophages and HepaRG hepatoma cells. *Int J Pharm*. 2016; 513: 438-52.
57. Sheng Y, Yuan Y, Liu C, Tao X, Shan X, Xu F. In vitro macrophage uptake and in vivo biodistribution of PLA-PEG nanoparticles loaded with hemoglobin as blood substitutes: effect of PEG content. *J Mater Sci Mater Med*. 2009; 20: 1881-91.
58. Qu J, Zhao X, Ma PX, Guo B. pH-responsive self-healing injectable hydrogel based on N-carboxyethyl chitosan for hepatocellular carcinoma therapy. *Acta Biomater*. 2017; 58: 168-80.